

Magnetic field noise cancellation for quantum simulation experiment with trapped ions

A master's thesis submitted to the
faculty of mathematics, computer science and physics
of the
University of Innsbruck
in partial fulfillment of the requirements for the degree of
Master of Science (MSc)
under the supervision of
Dr. Christian F. Roos

Johannes Franke

19th November 2021
carried out at the Institute for
QUANTUM OPTICS AND QUANTUM INFORMATION



Abstract

In this thesis a feed-forward compensation system for magnetic field noise at quantum experiments with trapped ions is presented. This compensation system is realised at two experimental set-ups, one for quantum simulations and the other for precision spectroscopy. In both experiments, the qubit is encoded in a pair of electronic levels of a trapped $^{40}\text{Ca}^+$ ion. The compensation system is used to suppress the ambient magnetic field noise in the laboratories induced by the 50 Hz power line. A simple technical approach is used for the feed-forward system based on magnetic field coils and a function generator to create a modulated magnetic field. The feed-forward compensation system works by applying an out-of-phase magnetic field to destructively superpose the magnetic field noise at the location of the ions. For the function generator, a programmable RedPitaya board is used. For this board a controlling software was developed within this work, which allows a fast operation of the compensation system. Furthermore an experimental sequence where the ion qubits are used as sensor for quantifying the magnetic field noise is developed. This experiment relies on the CPMG π -pulse sequence.

Zusammenfassung

In dieser Arbeit wird ein Feed-forward Kompensationssystem zur Unterdrückung von Magnetfeldstörungen bei quantenphysikalischen Experimenten mit gefangenen Ionen vorgestellt. Das System wurde erfolgreich an zwei unterschiedlichen experimentellen Aufbauten realisiert. Ein Aufbau wird für die Durchführung von Quantensimulationsexperimenten genutzt, wohingegen der andere der Präzisionsspektroskopie dient. In beiden Experimenten wird das Qubit in einem Paar elektronischer Zuständen eines $^{40}\text{Ca}^+$ Ions realisiert. Das Feed-forward System wird verwendet, um die durch die 50 Hz Netzspannung erzeugten Magnetfeldstörungen im Labor zu unterdrücken. Das System basiert auf Magnetfeldspulen und einem Funktionsgenerator zur Erzeugung eines modulierten Magnetfeldes. Die Kompensation wird dadurch erreicht, dass ein gegenphasiges Magnetfeld im Zentrum der Falle erzeugt wird und destruktiv mit der Magnetfeldstörung interferiert. Als Funktionsgenerator wird ein programmierbares RedPitaya Board verwendet. Zur einfacheren Bedienung des Kompensationssystems wurde eine Software entwickelt. Des Weiteren wurde eine Experimentsequenz entwickelt, die es ermöglicht die Magnetfeldstörung mit den Ionenqubit zu messen. Diese Sequenz basiert auf der CPMG π -Pulssequenz.

Contents

1. Introduction	7
2. Theoretical background	9
2.1. The Paul trap	9
2.2. Quantum bits	11
2.3. Two-level ion interacting with laser beam	14
2.4. Atomic structure of Ca^+	18
2.5. Laser cooling	19
3. Theory of measuring power line induced transition frequency shifts with a qubit	23
3.1. Dephasing noise and Ramsey experiments	23
3.2. π -pulse train and the CPMG sequence	28
3.3. Asynchronous noise	33
4. Experimental setup	35
4.1. Ion trap setup	35
4.2. Feed-forward system for noise cancellation	37
4.2.1. Characterisation of the coil system	37
4.2.2. Function generator system	39
5. Experimental compensation of magnetic field noise	42
5.1. Compensation of magnetic field noise at the QSIM experiment . . .	42
5.1.1. Characterisation of noise components with the Raman transition	42
5.1.2. Noise parameter fluctuation	48
5.1.3. Characterisation and compensation of noise components using the 729-transition	51
5.1.4. Ramsey contrast with and without compensation	52
5.2. Compensation of magnetic field noise at the Precision experiment .	54
5.2.1. Characterisation and compensation of noise components . .	54
5.2.2. Coherence measurement with Ramsey contrast	57
6. Conclusion and outlook	59

Appendix A. Derivation of the filter function	61
Appendix B. Controlling software for the Red Pitaya	65
B.1. Controlling software: Manual mode	65
B.2. Controlling software: Automated fit	66
B.3. Controlling software: Parameter window	69
Appendix C. Useful Formulas	70
C.1. Trigonometric functions	70
C.2. Pauli matrices	70
C.3. Annihilation and creation operator	71

1. Introduction

„And I’m not happy with all the analyses that go with just the classical theory, because nature isn’t classical, dammit, and if you want to make a simulation of nature, you’d better make it quantum mechanical, and by golly it’s a wonderful problem, because it doesn’t look so easy.”

With these words Richard Feynman ended his famous seminal lecture „Simulating Physics with Computers” in 1981 and introduced the idea of a quantum simulator [1]. In a quantum simulator, the quantum system of interest is simulated by another quantum system. The quantum system used for simulation has to be well-known and controllable. Following this concept, experiments based on different quantum systems have been developed to perform such simulations [2]: Trapped ions [3], cold atoms in optical lattices [4], superconducting circuits [5] and more, with all of them having different strengths and weaknesses. For quantum simulators two approaches can be distinguished: Analogue and digital quantum simulator. In the analogue approach the system of interest is directly mapped to the controllable simulation system. This limits the usage of an analogue quantum simulator to a particular set of problems [6]. The digital quantum simulator is a quantum system with a set of universal quantum operations (gates). In this approach the state of the system of interest is encoded in the quantum information carrier and the dynamics are simulated with sequence of quantum operations. This simulator can, to some extent, simulate any local quantum system, which makes the digital quantum simulator an universal simulator and similar to a quantum computer [7]. Ignacio Cirac and Peter Zoller theoretically proposed trapped ions as a platform for quantum computing [8]. In this system the ions serve as carrier for the quantum information and laser beams are used for manipulating and read out of the quantum information. Shortly afterwards the first quantum gate has been performed on a single ion [9]. Laser cooling allows the crystallisation of ions in the harmonic potential of the trap [10]. In such an ion crystal the internal energy levels as well as the vibrational modes can be exploit. In the group of Rainer Blatt in Innsbruck, the implementation of a quantum gate operation between two individual ions was realized in 2003 by coupling the ions through their quantized vibrational motion [11], and soon after three-qubit entangled states with ions have been created [12]. One advantage of using trapped ions is the possibility of controlling and measuring individual ions. In Innsbruck, the individual ion addressing

1. Introduction

has been recently realised in a quantum experiment with a long ion string with 51 ions [13]. Such a long ion string extends across a length of $200 - 300\mu\text{m}$.

An ideal quantum experiment would be perfectly isolated from the environment and controlled with very high precision. Unwanted influences from the environment lead to disturbance of the experiment. To achieve an unperturbed quantum system, it is one goal of quantum physicists to either design a setup providing an excellent isolation from the environment, or to introduce feedback or feed-forward mechanisms capable of compensating the disturbances. One of such disturbances is the ambient magnetic field in the laboratory. The ambient magnetic field is among others induced by electrical devices and power supplies. Especially the 50 Hz electricity mains (AC power line), powering the laboratory devices, produces an alternating magnetic field. Nonlinear loads lead to the occurrence of higher harmonics of 50 Hz. One example of such a nonlinear load are DC power supplies (single-phase diode bridge rectifier) commonly used in powering PCs and screens. These electrical devices disturb the harmonic signal and give rise to the odd higher harmonics of 50 Hz (150 Hz, 250 Hz, ...)[14]. For qubits whose transition frequency depends to first order on the strength of the magnetic field, the field leads to a shift of the transition frequencies of the ion. Magnetic field noise further leads to decoherence of the qubit [15]. Hence ion qubit experiments require an environment with low magnetic field noise.

In this master project, a feed-forward compensation system was developed to suppress magnetic field noise induced by the AC power line. On the technical side, the magnetic field noise compensation system is comprised of a pair of magnetic field coils and a function generator to generate a magnetic field in the center between the two coils. As a function generator, a RedPitaya STEMLab board is used. A software was developed to control the compensation system. It includes a graphic interface, which allows the user to operate the system manually as well as in a semi-automatic way. Furthermore experimental laser pulse sequences were developed to measure the magnetic field by sensing the modulation of the transition frequency of the ions. The sensing protocol makes use of CPMG sequences (after Carr, Purcell, Meiboom and Gill)[16], which are generalizations of the spin echo technique. With this sequence it is possible to measure noise with fixed frequencies. The compensation system was successfully implemented in two experiments: The quantum simulation experiment (QSIM) and the precision spectroscopy experiment (Precision).

2. Theoretical background

In this first theoretical section, the basic concepts of quantum experiments with trapped ions are introduced, starting with the principle of Paul traps. The second part focuses on quantum physics, especially quantum optics. Later the properties of Ca^+ , the ion species used in the experiment, are summarized. In the end of this section cooling of the ion is described in more detail.

2.1. The Paul trap

In order to trap charged particles, the confinement in all three directions has to be achieved. Because of the Laplace equation $\Delta\Phi = 0$, confinement in all three directions with a purely static electric field is not possible. To fulfill the equation, the curvature in at least one direction has to be negative. One solution to create confinement in all three directions consists in using an oscillating field, which is the operating principle of a Paul trap. [17]

Linear Paul traps and the classical dynamics of ions in the trap have been discussed in a couple of theses describing the QSIM setup and quantum experiments carried out with this setup (see [18, 19] or more at the QSIM page of quantu-moptics.at). In the following, the key principles are briefly summarized. The potential in the center of the trap can be approximated by an electric quadrupole field [20]

$$\Phi(x, y, z, t) = U_{RF} \cos(\Omega_{RF}t) \frac{\tilde{\alpha}x^2 + \tilde{\beta}y^2 + \tilde{\gamma}z^2}{2r_0^2} + U_{DC} \frac{\alpha x^2 + \beta y^2 + \gamma z^2}{2r_0^2} \quad (2.1)$$

with the RF-potential frequency Ω_{RF} , the amplitude U_{RF} and the static amplitude U_{DC} . The characteristic length scale r_0 is on the order of the distance between the ion and the trap electrodes. The dimensionless geometric factors α, β, γ and $\tilde{\alpha}, \tilde{\beta}, \tilde{\gamma}$ account for geometric differences between the electrodes of a real trap and ideal hyperbolic electrodes [18]. The geometric factors have to satisfy the Laplace equation. In the linear trap configuration a static field is applied to the tip electrodes, as drawn in figure 2.1 (a), and the oscillating field to a pair of blade electrodes. This yields the condition for the geometric factors $-(\alpha + \beta) = \gamma > 0$, $\tilde{\alpha} = -\tilde{\beta}$ and $\tilde{\gamma} = 0$, to trap positive ions in an ideal linear Paul trap. The classical equation of motion of a particle with charge Q and mass m is obtained by the

2. Theoretical background

differential equation $m\ddot{\vec{r}} = -\nabla Q\Phi(\vec{r}, t)$. The motion of an ion governed by this equation is given by three uncoupled differential equations for the ion's coordinates, with the formula for the x direction

$$\frac{d^2x}{d\zeta^2} + (a_x - 2q_x \cos(2\zeta))x = 0, \quad (2.2)$$

where the other coordinates can be treated analogously. The equation has the form of the Mathieu differential equation with the dimensionless parameters q , a and ζ [21]

$$\zeta = \frac{\Omega_{RF}t}{2}, \quad q_x = \frac{4\tilde{\alpha}QU_{RF}}{m\Omega_{RF}^2r_0^2} = -q_y, \quad a_x = \frac{2\alpha QU_{DC}}{m\Omega_{RF}^2r_0^2} = a_y = -\frac{a_z}{2}. \quad (2.3)$$

This equation can be solved with the Floquet theorem with a general solution $x(t) = e^{-i\beta_x\zeta}u(\zeta)$ including a periodic function $u(\zeta)$ and the characteristic exponent $\beta_x(a_x, b_x)$, which is a function of the parameters a and b . In the case β_x is real, the trajectory is stable (blue/red shaded areas in graph 2.1(b)) and for a complex β_x the trajectory is unstable. For the lowest stability zone shown in figure 2.1(d), the ion's trajectory can be approximated for $a_x, q_x \ll 1$ by

$$x(t) \approx A \cos(\omega_x t) \left(1 - \frac{q_x}{2} \cos(\Omega_{RF}t) \right) \quad (2.4)$$

with an amplitude A [20]. The ion performs a harmonic motion with the frequency $\omega_x = \frac{\Omega_{RF}}{2} \sqrt{\frac{q_x^2}{2} + a_x}$, which is called *secular motion*. On top of that the ion oscillates with the RF-potential frequency, this is called *micro motion*. In order that the secular frequency does not become imaginary and the ion does not follow an unstable trajectory, the lower bound for the a_x parameter is $\frac{q_x^2}{2} > -a_x$. This is shown in the first stability zone in figure 2.1(d) by the lowest blue curve. Similar, an upper bound for a_y can be found by using the relation (2.3) $\frac{q_y^2}{2} > a_y$, which is the upper red curve in figure 2.1 (d). To confine the ion in both directions the trapping parameters have to be chosen such that a and q lay in the region between the two curves.

The equation of motion (2.4) is obtained by carrying out the *secular approximation*, where the location of the ion $x(t) = \bar{x}(t) + \xi(t)$ is split in a slow varying part \bar{x} and a fast one ξ . This allows to separate the differential equation to $m\ddot{\xi}(t) = -\partial_x Q\Phi(\bar{x}, t)$ and for the slow varying part $m\ddot{\bar{x}}(t) = \langle -\partial_x Q\Phi(\bar{x}, t) \rangle$ with the time average of the force. Therefore the secular frequency $\omega_x \ll \Omega_{RF}$ has to be smaller than the driven frequency, which is comparable to the condition for equation (2.4).

2. Theoretical background

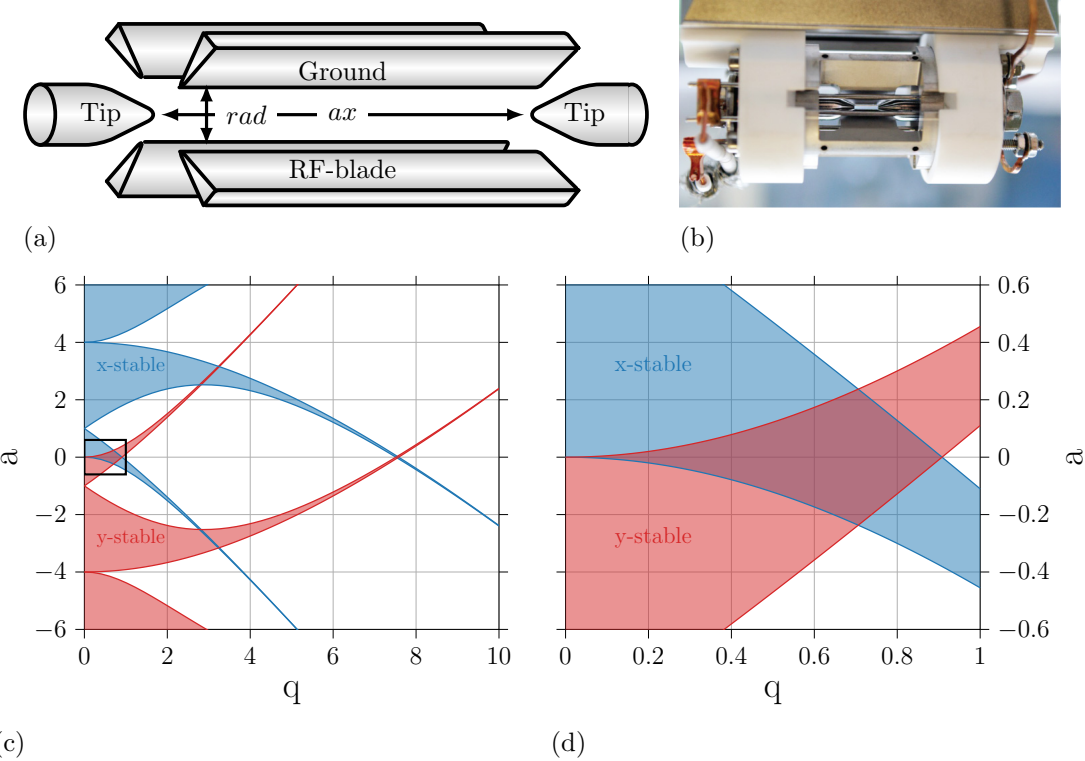


Figure 2.1.: Linear Paul trap

Graphic (a) illustrates the geometry of a linear Paul trap. The radial blades create a RF-potential in the x-y plane (rad). The tips create a static potential along the z-axis (ax). The photo in (b) shows the trap used in the QSIM experiment. Here the two tip electrodes and two of the four blade electrodes can be seen. In front of the trapping electrodes are the electrodes for compensating the micro motion (see text to equation (2.4)). The photo is taken from [18]. The lower graphs show the stability diagram for the solution of the Mathieu equation (2.2). The stability diagrams are created by calculating the characteristic parameters with the python functions `mathieu_a` and `mathieu_b` from the library `scipy.special` [22]. The ion trajectory is stable for values of the parameters a , q in the shadowed area (red for y confinement and blue for x confinement). Confinement in both directions is achieved by choosing parameters in the cross section of the red and blue graphs. The graphic (d) shows a zoom in the lowest stability region. Close to the origin (i.e. $a_x, q_x \ll 1$) the trajectory can be approximated by equation (2.4).

2.2. Quantum bits

The basic building block for classical computing is the bit. Analogous to this classical bit one can introduce the *quantum bit*, or short *qubit*. A qubit is comprised of two states, $|0\rangle$ and $|1\rangle$ of a quantum mechanical two-level system or also called

2. Theoretical background

spin- $\frac{1}{2}$ system.¹ Compared to the classical bit state, which can be either 0 or 1, the qubit can also be in a superposition state $|\psi\rangle = \alpha|\downarrow\rangle + \beta|\uparrow\rangle$. The complex coefficients of the linear combination α and β are called the probability amplitude. They provide information of the probability to find the state in $|\uparrow\rangle$ with a probability $|\beta|^2$, or in $|\downarrow\rangle$ with a probability $|\alpha|^2$ after a measurement. Due to the fact that the coefficients represent a probability they are normalized such that the equation $|\alpha|^2 + |\beta|^2 = 1$ holds. Using these properties the state of a qubit can be represented as a vector in a two-dimensional complex vector space. This vector space is spanned by the *computational basis* vectors $|\downarrow\rangle = \begin{pmatrix} 0 \\ 1 \end{pmatrix}$ and $|\uparrow\rangle = \begin{pmatrix} 1 \\ 0 \end{pmatrix}$. This geometrical representation of the qubit state can be achieved by using spherical coordinates

$$|\psi\rangle = e^{i\gamma} \left(\cos\left(\frac{\theta}{2}\right) |\uparrow\rangle + e^{i\varphi} \sin\left(\frac{\theta}{2}\right) |\downarrow\rangle \right) \quad (2.5)$$

with the azimuthal angle φ and the polar angle θ . The global phase γ can be neglected, because in general we are interested in measurement outcomes, which are calculated by the absolute square of the state projected to the measurement basis $P_{\uparrow} = |\langle \uparrow | \psi \rangle|^2$. Hence the global phase is not measurable by measuring the probability in a two-level system. In the case of a multi level system, e.g. 3-level-system, the phase γ of the two states matters. Figure 2.2 shows this representation on the so called *Bloch sphere*. The basis vectors are set to the poles of the sphere and the superposition states $|\pm\rangle_x = 1/\sqrt{2}(|\uparrow\rangle \pm |\downarrow\rangle)$ and $|\pm\rangle_y = 1/\sqrt{2}(|\uparrow\rangle \pm i|\downarrow\rangle)$ are set to the x- and y-axis. [23]

The qubit itself is not sufficient for computing, operations, or more precisely the manipulation of the qubit by gates is needed. Single qubit operations can be described by rotations of the state vector on the Bloch sphere. Treating the qubit as a (pseudo) spin- $\frac{1}{2}$ system, the cartesian components of the spin observable are described by the Pauli matrices

$$\sigma_x = \begin{pmatrix} 0 & 1 \\ 1 & 0 \end{pmatrix} \quad \sigma_y = \begin{pmatrix} 0 & -i \\ i & 0 \end{pmatrix} \quad \sigma_z = \begin{pmatrix} 1 & 0 \\ 0 & -1 \end{pmatrix} \quad (2.6)$$

with the eigenvectors $|\uparrow\rangle$ and $|\downarrow\rangle$ for σ_z , $|\pm\rangle_x$ for σ_z and $|\pm\rangle_y$ for σ_y . A rotation around the z-axis by an angle θ is then mathematically described by the rotation operator using σ_x

$$\mathcal{U}_z(\theta) = e^{-i\frac{\theta}{2}\sigma_z} = \cos\left(\frac{\theta}{2}\right) \mathbf{1} - i \sin\left(\frac{\theta}{2}\right) \sigma_z = \begin{pmatrix} e^{-i\frac{\theta}{2}} & 0 \\ 0 & e^{i\frac{\theta}{2}} \end{pmatrix}. \quad (2.7)$$

¹In this work the convention $|0\rangle = |\downarrow\rangle$ ($|1\rangle = |\uparrow\rangle$), referred to the spin-1/2 system, is used in order to not confuse with the Fock states $|0\rangle, \dots |n\rangle$.

2. Theoretical background

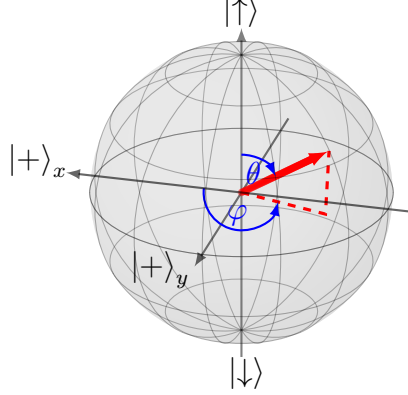


Figure 2.2.: Bloch sphere

The Bloch sphere is a way to illustrate the quantum mechanical two-level system. The eigenstates $| \uparrow \rangle$ and $| \downarrow \rangle$ are set to the poles of the sphere and the superposition states to the x-,y-axis. The state vector is presented in red with its spherical coordinates θ and φ .

Here Euler's formular (see C) is used. A rotation around an axis in the x-y-plane is described by the rotation operator

$$\begin{aligned} \mathcal{U}_\varphi(\theta, \varphi) &= e^{-i\frac{\theta}{2}\sigma_\varphi} = \cos\left(\frac{\theta}{2}\right)\mathbb{1} - i\sin\left(\frac{\theta}{2}\right)\sigma_\varphi \\ &= \begin{pmatrix} \cos\left(\frac{\theta}{2}\right) & -ie^{-i\varphi}\sin\left(\frac{\theta}{2}\right) \\ -ie^{i\varphi}\sin\left(\frac{\theta}{2}\right) & \cos\left(\frac{\theta}{2}\right) \end{pmatrix} \end{aligned} \quad (2.8)$$

with $\sigma_\varphi = \cos(\varphi)\sigma_x + \sin(\varphi)\sigma_y$. For example, a rotation by an angle $\theta = \pi$ around $|+⟩_y$ performs a spin flip from $| \downarrow \rangle$ to $| \uparrow \rangle$ as illustrated in 2.3(a)

$$\mathcal{U}_\varphi\left(\pi, \frac{\pi}{2}\right)| \downarrow \rangle = \left[\cos\left(\frac{\pi}{2}\right)\mathbb{1} - i\sin\left(\frac{\pi}{2}\right)\sigma_y\right]| \downarrow \rangle = -| \uparrow \rangle.$$

A rotation by $\theta = \frac{\pi}{2}$ around $|x\rangle_+$ rotates the state $| \downarrow \rangle$ into the equatorial plane as illustrated in 2.3(b)

$$\mathcal{U}_\varphi\left(\frac{\pi}{2}, 0\right)| \downarrow \rangle = \left[\cos\left(\frac{\pi}{4}\right)\mathbb{1} - i\sin\left(\frac{\pi}{4}\right)\sigma_x\right]| \downarrow \rangle = -i\frac{1}{\sqrt{2}}(| \uparrow \rangle + i| \downarrow \rangle) \equiv |+⟩_y.$$

As described previously the global phase i or -1 can be neglected.

In the real experiment, measurement results are obtained by averaging over n quantum projection measurements. The standard deviation of the obtained outcome $\langle P_{\uparrow} \rangle$ is

$$\Delta P_{\uparrow} = \sqrt{\frac{P_{\uparrow}(1-P_{\uparrow})}{n}}, \quad (2.9)$$

which is called *quantum projection noise* [24].

2. Theoretical background

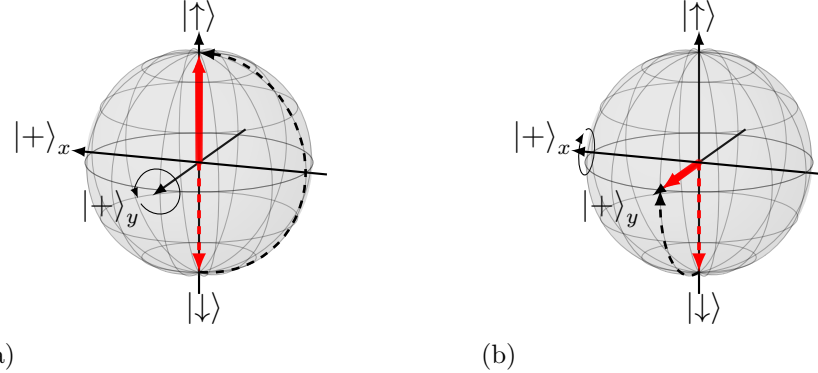


Figure 2.3.: Rotation on the Bloch sphere

The first Bloch sphere (a) illustrates a spin flip, where the state vector in red is rotated around the y-axis from $|\downarrow\rangle$ to $|\uparrow\rangle$. In the second Bloch sphere (b) a quarter rotation of the state vector to the state $|+\rangle_y$ is shown.

2.3. Two-level ion interacting with laser beam

In this section the interaction of a trapped ion with a laser beam is introduced. Here, the ion is treated as two-level system assuming that only two levels of the ion are coupled by the laser.

The ion's motion in the trapping potential is represented as a quantized one-dimensional harmonic oscillator. Similar to the classical case, the energy of a particle in a harmonic potential is the sum of the kinetic energy $E_{kin} = \hat{p}^2/2m$ and the potential energy $V = 1/2mv^2\hat{x}^2$ of the harmonic potential with the momentum operator \hat{p} and the space operator \hat{x} . Using the ladder operators, which were first introduced by Dirac [25], we can rewrite the operators

$$\hat{x} = \underbrace{\sqrt{\frac{\hbar}{2m\nu}}}_{x_0} (a^\dagger + a) \quad \text{and} \quad \hat{p} = i\sqrt{\frac{\hbar m\nu}{2}} (a^\dagger - a). \quad (2.10)$$

With these operators, the Hamiltonian of the harmonic oscillator can be expressed as

$$\mathcal{H}_T = \hbar\nu (a^\dagger a + 1/2), \quad (2.11)$$

where the product of the ladder operators $N = a^\dagger a$ is called number operator. The eigenvectors of the number operator $N |n\rangle = n |n\rangle$ are the *Fock states*. Due to the fact that the Hamiltonian is linear dependent on N the Fock states are also eigenstates of the harmonic oscillators. These states describe the discrete motional states of the ion in the trap with an energy separation of $\hbar\nu$. Their eigenvalues $n \in \mathbb{N}$ correspond to the number of excitation in the harmonic oscillator, also

2. Theoretical background

called number of motional quanta or phonons. As illustrated in figure 2.4(a), the annihilation operator a destroys a phonon, whereas the creation operator a^\dagger creates a phonon.

The internal degrees of freedom of the ion are described by the Hamiltonian

$$\mathcal{H}_A = \frac{\hbar\omega_0}{2}\sigma_z, \quad (2.12)$$

where the basis vectors of σ_z are the ground state $|\downarrow\rangle$ and the excited state $|\uparrow\rangle$ of the system and $\hbar\omega_0$ is the energy difference between the states. This definition assumes that the zero point of the energy is set half-way between the energy of the two states. A laser beam changes the state of the ion. This can be described by the Hamiltonian

$$\mathcal{H}_l = \hbar\Omega \cos(kx - \omega_l t + \varphi_l) \sigma_x \quad (2.13)$$

with the laser properties given by the wave vector k , the laser frequency ω_l and the laser phase φ_l . The coupling strength between the laser and the ion is described by the Rabi frequency Ω . To illustrate the interaction between the ion and the laser, a transformation to the interaction picture with respect to $\mathcal{H}_0 = \mathcal{H}_A + \mathcal{H}_T$ with $\mathcal{U}_0 = \exp(-i/\hbar\mathcal{H}_0 t)$ is performed:

$$\begin{aligned} \mathcal{H}_I &= \mathcal{U}_0^\dagger \mathcal{H}_{AF} \mathcal{U}_0 \\ &= \frac{\hbar\Omega}{2} e^{i\nu t a^\dagger a} \left(e^{i\eta(a^\dagger + a)} e^{-i(\omega_l t - \varphi_l)} + c.c. \right) e^{-i\nu t a^\dagger a} e^{\frac{i\omega_0 t}{2}\sigma_z} \sigma_x e^{-\frac{i\omega_0 t}{2}\sigma_z}. \end{aligned} \quad (2.14)$$

The space component is rewritten as $x = x_0 (a + a^\dagger)$, introducing the Lamb-Dicke parameter²

$$\eta = k \sqrt{\frac{\hbar}{2m\nu}}. \quad (2.15)$$

This parameter describes the ratio between the size of the ground state wave packet of the harmonic oscillator and the wavelength of the laser. It is a measure for the comparison of the laser length scale with the ion wave packet. Using the properties of the Pauli matrices and the ladder operators, the interaction Hamiltonian (see Appendix C) can be further simplified

$$\mathcal{H}_I = \frac{\hbar\Omega}{2} \left(e^{i\eta(\hat{a}^\dagger + \hat{a})} e^{-i(\omega_l t - \varphi_l)} + c.c. \right) (\cos(\omega_0 t) \sigma_x - \sin(\omega_0 t) \sigma_y), \quad (2.16)$$

where $\hat{a}^\dagger = a^\dagger e^{i\nu t}$ is the time-dependent creation operator. Introducing the detuning $\Delta = \omega_l - \omega_0$ of the laser frequency from the frequency of the atomic transition

²In more dimensions the overlap between the axis i of the harmonic oscillator and the wave vector has to be calculated $\eta = \vec{k} \cdot \hat{e}_i \sqrt{\hbar/2m\nu_i}$

2. Theoretical background

the *rotating wave* approximation, where the rapidly oscillating terms $\omega_l + \omega_0$ are neglected, simplifies the Hamiltonian to

$$\mathcal{H}_I = \frac{\hbar\Omega}{2} \left(e^{i\eta(\hat{a}^\dagger + \hat{a})} e^{-i(\Delta t - \varphi_l)} \sigma_+ + e^{-i\eta(\hat{a}^\dagger + \hat{a})} e^{i(\Delta t - \varphi_l)} \sigma_- \right). \quad (2.17)$$

Here the ladder operators for the two-level system $\sigma_\pm = 1/2(\sigma_x \pm i\sigma_y)$ are used. The laser couples the motion of the ion in the trap with the internal state of the ion, if the detuning corresponds to $\Delta = m\nu$, the motional transition $|\downarrow, n\rangle \leftrightarrow |\uparrow, n+m\rangle$ takes place. In the Lamb-Dicke regime, defined by $k^2\sigma^2(\hat{x}) = \eta^2(2\bar{n} + 1) \ll 1$, the wave packet of the ion in the trap is smaller than the laser wavelength.³ In this case the exponential function can be Taylor-expanded into

$$e^{i\eta(\hat{a}^\dagger + \hat{a})} = \mathbb{1} + i\eta(\hat{a}^\dagger + \hat{a}) - \frac{\eta^2}{2}(\hat{a}^\dagger + \hat{a})^2 + \dots \quad (2.18)$$

and truncated after a few terms. Due to the fact that in the Lamb-Dicke regime the transitions, which change the motional quanta by $\Delta n > 1$, are suppressed [26], terms which include $\hat{a}^\dagger \hat{a}^\dagger$ or $\hat{a} \hat{a}$ are neglected. Using the Taylor expansion in formula (2.17) there are three transitions that can be excited by choosing the corresponding detuning Δ .

- The carrier transition, where the detuning is $\Delta = 0$, does not change the motinonal quanta $|\downarrow, n\rangle \leftrightarrow |\uparrow, n\rangle$. The corresponding interaction Hamiltonian is $\mathcal{H}_I = \hbar\Omega_c/2(e^{-i\varphi_l} |\uparrow, n\rangle \langle \downarrow, n| + e^{i\varphi_l} |\downarrow, n\rangle \langle \uparrow, n|)$ with the effective coupling strength $\Omega_c = \Omega(1 - \eta^2 n)$.
- In the case that the detuning $\Delta = \nu$ corresponds to the trap frequency the motional quanta is changed by $\Delta n = +1$ and the transition $|\downarrow, n\rangle \leftrightarrow |\uparrow, n+1\rangle$ takes place. This is also called blue-sideband transition, with its reduced Hamiltonian $\mathcal{H}_I = i\hbar\Omega_b/2(e^{-i\varphi_l} |\uparrow, n+1\rangle \langle \downarrow, n| - e^{i\varphi_l} |\downarrow, n\rangle \langle \uparrow, n+1|)$. The coupling strength is modified to $\Omega_b = \eta\sqrt{n+1}\Omega$.
- For the detuning $\Delta = -\nu$ a transition $|\downarrow, n\rangle \leftrightarrow |\uparrow, n-1\rangle$ takes place. This is the so called red-sideband transition with an interaction Hamiltonian of the form $\mathcal{H}_I = i\hbar\Omega_r/2(e^{-i\varphi_l} |\uparrow, n-1\rangle \langle \downarrow, n| - e^{i\varphi_l} |\downarrow, n\rangle \langle \uparrow, n-1|)$. The effective coupling strength for this transition is $\Omega_r = \eta\sqrt{n}\Omega$.

The interaction between an ion and a laser pulse is described by the unitary time evolution operator $\mathcal{U}(\theta, \varphi_l) = \exp\left(\frac{-i\mathcal{H}_I t}{\hbar}\right)$. For the case of the carrier transition, the time evolution operator has the form

$$\mathcal{U}(\theta, \varphi_l) = \cos\left(\frac{\theta}{2}\right) \mathbb{1} - i \sin\left(\frac{\theta}{2}\right) (e^{-i\varphi_l} \sigma_+ + e^{i\varphi_l} \sigma_-) \quad (2.19)$$

³The size of the wave packet is calculated $\sigma^2(\hat{x}) = \langle \hat{x}^2 \rangle - \langle \hat{x} \rangle^2$ with $\langle \hat{x} \rangle = \langle \psi | \hat{x} | \psi \rangle$

2. Theoretical background

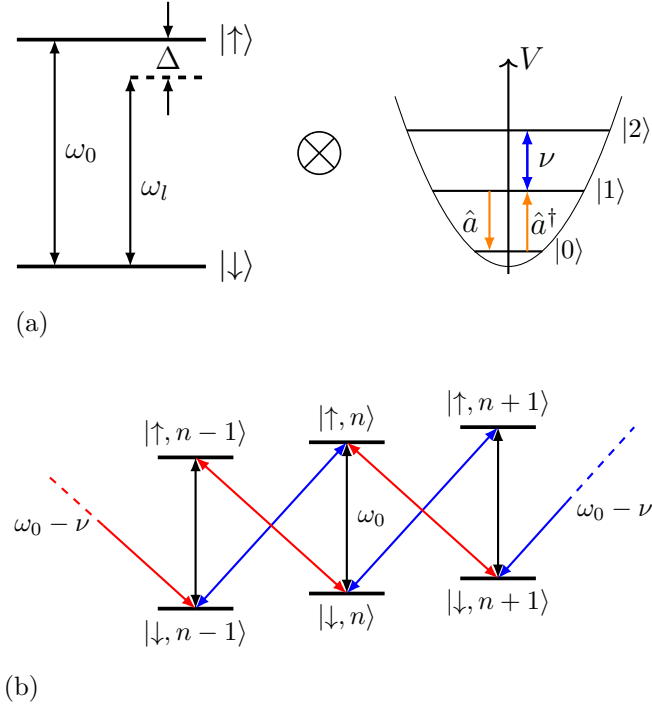


Figure 2.4.: Level diagram of two-level system and QM harmonic oscillator
The illustration (a) shows the internal states and the motional states. The energy levels of the two-level system with ground state $|\downarrow\rangle$ and excited state $|\uparrow\rangle$ are separated by the energy $\hbar\omega_0$. Additionally the laser frequency ω_l with the detuning Δ from the energy level is drawn. The second part shows the levels of the harmonic oscillator separated by $\hbar\nu$ and the Fock states $|0\rangle, \dots, |n\rangle$. The creation (annihilation) of a phonon by application of the ladder operators \hat{a}^\dagger (\hat{a}) are shown with arrows. The combined energy levels of the two-level system and the harmonic oscillator and the transitions are presented in (b). The carrier transition between the states $|\downarrow, n\rangle \leftrightarrow |\uparrow, n\rangle$, drawn in black, is separated by ω_0 . The two sidebands separated by $\omega_0 \pm \nu$, which correspond to the transition $|\downarrow, n\rangle \leftrightarrow |\uparrow, n \pm 1\rangle$, are drawn in their corresponding color between the states.

2. Theoretical background

with the *pulse area* $\theta = \Omega t$. This corresponds to a rotation on the Bloch sphere with a rotation axis set by the laser phase ϕ and the rotation angle by the pulse area θ as described in the section before. From this we get two important classes of laser pulses.

- The π -pulse, where the pulse area is $\Omega t = \pi$, transfers the ion from the ground to the excited state $|\downarrow\rangle \rightarrow |\uparrow\rangle$ (or vice versa).
- The pulse, which transfers the ion from the ground to the superposition state, is called $\frac{\pi}{2}$ -pulse because the pulse area equals $\Omega t = \frac{\pi}{2}$.

2.4. Atomic structure of Ca^+

In this experiment the cation of the earth alkali atom calcium Ca^+ is used. The most common isotopes with abundance 97% and 2% [27] are ^{40}Ca and ^{44}Ca . Both ions have zero nuclear spin, therefore no hyperfine splitting, which simplifies the level scheme of the ions. As the ion has one valence electron, it has a level structure similar to the one of alkali atoms. A two-step photoionization of neutral calcium atoms enables isotope-selective loading of ions into the trap. Thereby a tuneable 422 nm laser, which is tuned to the frequency of which selects the isotope to be loaded, is used to excite one electron from the ground state $4s^2 \ ^2S_0$ of neutral calcium to the state $4s4p^2P_1$. In the second step the atom is ionized using a 375 nm laser. The level scheme of $^{40}\text{Ca}^+$ is shown in figure 2.5. An external magnetic field $B(t)$ gives rise to a splitting of the fine structure-levels into $2j + 1$ Zeeman sublevels. For the low magnetic fields used in the experiments, this so called Zeeman-effect shifts the energy of a transition by

$$\Delta(t) = \frac{\mu_B}{\hbar} \underbrace{\left(g'_j m'_j - g_j m_j \right)}_{\gamma} B(t) \quad (2.20)$$

with the Bohr magneton μ_B , the Landé g-factors g_j and the magnetic quantum numbers m_j, m'_j of each state.⁴ In this master thesis two different approaches for encoding a qubit in a Ca^+ ion were employed, where the qubit is encoded in different states. The first system, called the optical qubit, uses the quadrupole transition between the ground state $|\downarrow\rangle \equiv |4^2S_{1/2}, m = 1/2\rangle$ and $|3^2D_{5/2}, m = 5/2\rangle$ as excited state $|\uparrow\rangle$. Using the above formula with $g_j(S_{1/2}) \approx 2$ and $g_j(S_{5/2}) \approx 1.2$ gives a magnetic field sensitivity $\gamma = 2$ for this transition. The second system, called ground state qubit, uses a Raman transition and the qubit is encoded in $|4^2S_{1/2}, m = -1/2\rangle \equiv |\downarrow\rangle$ and $|4^2S_{1/2}, m = 1/2\rangle \equiv |\uparrow\rangle$. The magnetic field sensitivity is basically the same to the value for the quadrupole transition.

⁴useful value $\mu_B/\hbar \approx 2\pi \cdot 1.399 \text{ MHz/G}$

2. Theoretical background

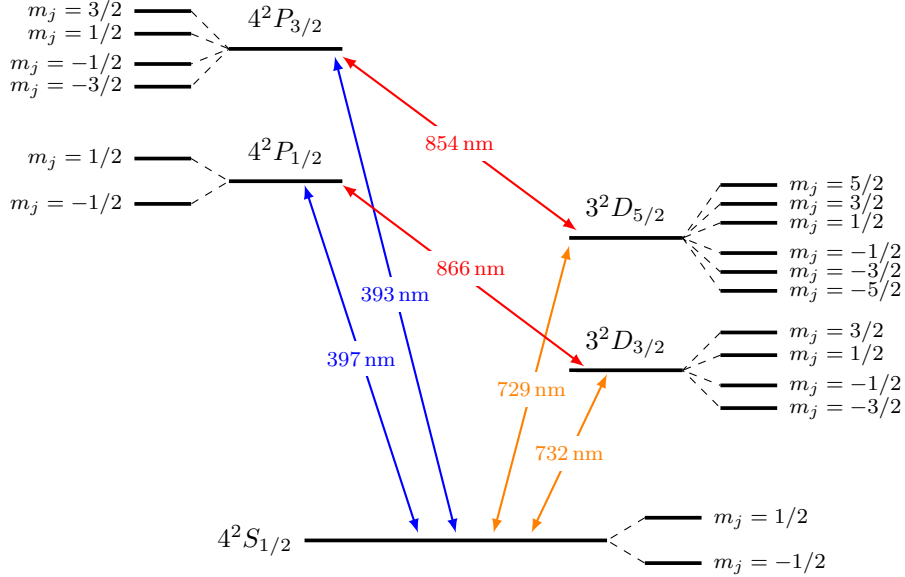


Figure 2.5.: Level diagram of Ca^+

The diagram shows the relevant levels and transition wavelengths of $^{40}\text{Ca}^+$. The qubit is encoded in the Zeeman sublevels of $4^2S_{1/2}$ and $3^2D_{5/2}$. The values for the transition wavelengths are taken from [27].

2.5. Laser cooling

To work with ion qubits, the ions should ideally be in the motional ground state. To cool hot ions, two cases can be distinguished. In the first case the hot ions have a linewidth Γ broader than the trap frequency ν , i.e. $\nu \ll \Gamma$. In this case the linewidth is broader than the spacing of the oscillator levels, which results in unresolved sidebands. The cooling process used in this state is Doppler cooling. In the latter case the ion linewidth is smaller than the trap frequency $\nu \geq \Gamma$ and the sidebands become resolved. This property enables cooling of the ions by selective excitation of the red sideband; accordingly, the cooling process has been named sideband cooling.[20, 28]

The absorption of a photon gives the ion a momentum kick in the direction of the laser k vector. The spontaneous emission does not change the ion's momentum on average, because it takes place in a random direction. The average kinetic energy change $E_{rec} = \hbar^2 k^2 / 2m$ given by this recoil can be related to the trap frequency ν via

$$\eta^2 = \frac{E_{rec}}{\hbar\nu} = \frac{\hbar k^2}{2m\nu} \quad (2.21)$$

the Lamb-Dicke parameter (2.15). In the Lamb-Dicke limit $\eta \ll 1$ the energy change caused by the photon is way smaller than the energy of a motional quanta,

2. Theoretical background

which is then the case for resolved and unresolved sidebands. In this limit the effect of cooling (and heating) can not be explained by the classical picture of Doppler cooling, as used for atomic gases, but with cooling via the sidebands by changing the motional quanta. For ions at room temperature the mean motional quantum number is $\bar{n} \approx 10^6$, which is not in the Lamb-Dicke regime, and transitions, which change the motional quanta by $\Delta n < 1$, are more likely [26]. While in the regime of unresolved sidebands, the direct addressing of particular sidebands with the laser is not possible (see figure 2.6(a)), which is possible in the resolved sideband regime $\nu \geq \Gamma$ (see figure 2.6(b)), the underlining mechanism is the same. In the following the cooling dynamics (in the Lamb-Dicke regime) are described by a rate equation model that considers transitions between neighboring motional states. The photon scattering rate

$$R = \Gamma \rho_{ee} = \Gamma \left(\frac{\Omega}{\Gamma} \right)^2 \underbrace{\frac{1}{1 + \left(\frac{2\Delta}{\Gamma} \right)}}_{W(\Delta)} \quad (2.22)$$

is given by the decay rate Γ of the excited state and the excited state probability ρ_{ee} with the line profile $W(\Delta)$ in the small intensity limit $\Omega \ll \Gamma$. There are two ways, to get from the state $|\downarrow, n\rangle \rightarrow |\downarrow, n-1\rangle$ shown in figure 2.6(c). The first is absorption on the carrier transition with a probability $(\Omega/\Gamma)^2 W(\Delta)$ and emission on the sideband with the rate $(n^2 \eta \Gamma)$. The second way is absorbing on the red sideband with probability $(n\sqrt{\eta} \Omega/\Gamma)^2 W(\Delta - \nu)$ followed by emission on the carrier transition with the rate Γ . The rates of both processes can be added up to the cooling rate

$$R_- = n\eta^2 \frac{\Omega^2}{\Gamma} (W(\Delta - \nu) + W(\Delta)). \quad (2.23)$$

The heating rate R_+ can be derived analogously. The rate coefficient $A_+ = (n + 1)R_+$ and $A_- = nR_-$ are

$$A_{\pm} = \frac{\eta^2 \Omega^2}{\Gamma} (W(\Delta \mp \nu) + W(\Delta)). \quad (2.24)$$

The steady state solution $\bar{n} = A_+/(A_- + A_+)$ for the mean vibrational number is reached when heating and cooling processes are balanced. To reach a small phonon number \bar{n} the ratio $\frac{A_-}{A_+}$ between the cooling rate and heating rate coefficient should be maximum. In the regime of unresolved sidebands, the maximum is reached for a laser detuning $\Delta = -\frac{\Gamma}{2}$ independent of the trap frequency. The minimal motional quantum $\bar{n} \approx \frac{\Gamma}{2\nu}$ number is then similar to the Doppler cooling limit of atomic gases. In the case of resolved sidebands, the laser can directly address the sideband with the detuning $\Delta = -\nu$. In the regime $\nu \gg \Gamma$ the motional quantum number $\bar{n} \approx \frac{\Gamma^2}{\nu^2}$ can be reached.[29]

2. Theoretical background

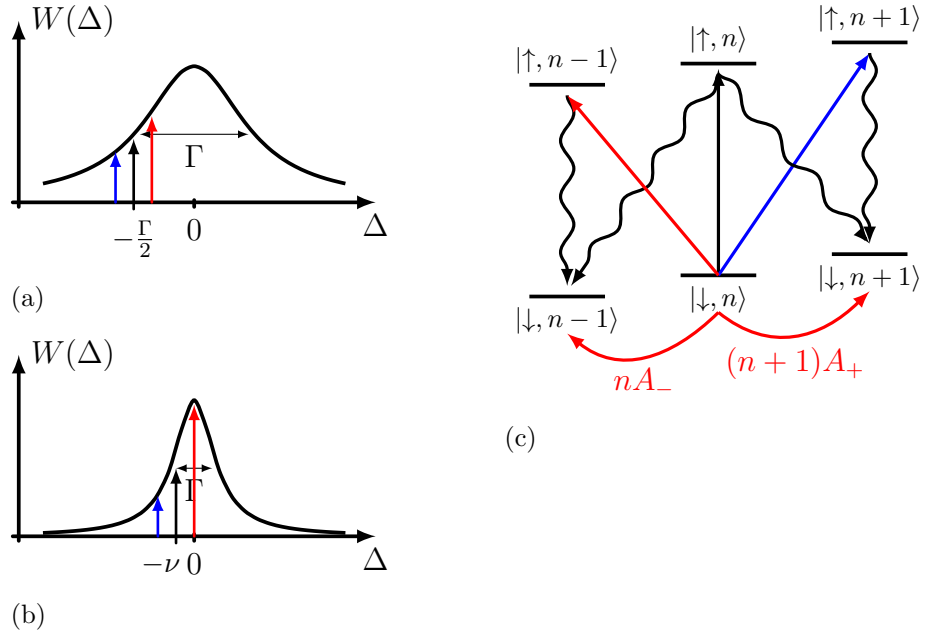


Figure 2.6.: Mechanism of laser cooling

Figure (a) and (b) show the line profile $W(\Delta)$ for weak confinement $\nu \ll \Gamma$ (a) and strong confinement $\nu \geq \Gamma$. The black arrows denote the carrier absorption for the optimum laser detuning $\Delta = \frac{-\Gamma}{2\nu}$ ($\Delta = -\nu$). The red arrows assign the red sideband absorption, which is stronger than the carrier and blue sideband absorption (blue arrows). The level diagram (c) shows the relevant transition for the cooling (heating) process. For details see text.

2. Theoretical background

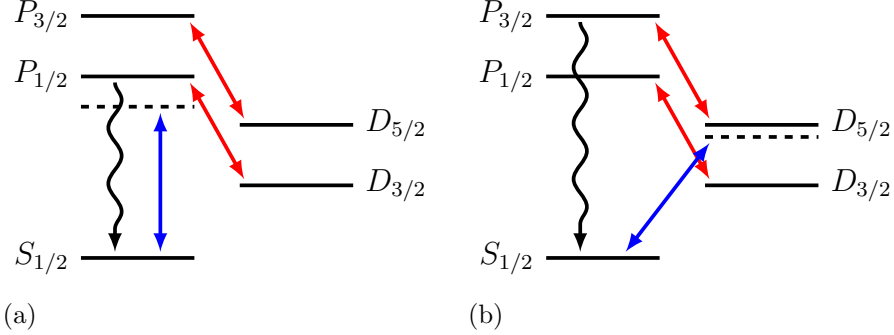


Figure 2.7.: Laser cooling of Ca^+

Diagram (a) shows the relevant levels for Doppler cooling and (b) the levels for sideband cooling.

Doppler cooling of the Ca^+ ion is performed on the $S_{1/2} \leftrightarrow P_{1/2}$ transition (see figure 2.7(a)). In order that the ion does not get pumped into one of the D states, an additional laser exciting the $D_{3/2} \leftrightarrow P_{1/2}$ transitions returns population from the $D_{3/2}$ state into the cooling cycle. Similarly, another laser exciting the $D_{5/2} \leftrightarrow P_{3/2}$ transition is available for pumping out population from the $D_{5/2}$ level. With a linewidth $\Gamma = (2\pi) 23 \text{ MHz}$ of the $P_{1/2}$ state and a trap frequency of $\nu = (2\pi) 1 \text{ MHz}$ a mean motional quantum number $\bar{n} \approx 10$ is expected at the Doppler limit. With a Lamb-Dicke parameter $\eta_{397} = 0.19$ for the $S_{1/2} \leftrightarrow P_{1/2}$ transition the Lamb-Dicke regime $\eta_{397}^2 \bar{n} < 1$ is reached [26].

Resolved sideband cooling is performed on the $S_{1/2} \leftrightarrow D_{5/2}$ transition (see figure 2.7(b)). Due to the long natural lifetime $\tau \approx 1 \text{ s}$ of the $D_{5/2}$ state, the lifetime is artificially shortened by driving the $D_{5/2} \leftrightarrow P_{3/2}$ transition. Additionally, the $D_{3/2} \leftrightarrow P_{1/2}$ is driven, so the ion does not get pumped into the $D_{3/2}$ state.[18]

3. Theory of measuring power line induced transition frequency shifts with a qubit

In this section we take a look at the influence of dephasing noise on the quantum states of a two-level system. For the QSIM experiment, the noise is mostly created by the ambient magnetic field in the laboratory. The 50 Hz AC mains powering the laboratory devices produces an alternating magnetic field. Nonlinearities in the electrical loads can lead to noise components of higher harmonics of 50 Hz. Here two cases can be distinguished: synchronous and asynchronous noise. Noise at multiples of 50 Hz can be turned into a deterministic variation of transition frequency shift by synchronising the experiment with the AC mains frequency. This is treated in the first two chapters. In the second chapter a way of quantifying these noise components with the help of a sequence of multiple π laser pulses (π -pulse train) applied to the two-level system is shown. The case of asynchronous noise is discussed in the last chapter.

3.1. Dephasing noise and Ramsey experiments

Assuming the Hamiltonian

$$\mathcal{H}_N(t) = \frac{\hbar}{2} \Delta(t) \sigma_z \quad (3.1)$$

with $\Delta(t)$ representing the time-dependent noise. In this case the noise is given by a magnetic field $B(t)$, which leads to a shift in the energy levels due to the Zeeman effect described by formula (2.20)

To evaluate the influence of the noise on a qubit, the time evolution operator in the interaction picture is calculated as described in the previous chapter. Due to the condition that the Hamiltonian is time-dependent and commutes with itself at different times $[\mathcal{H}(t_1), \mathcal{H}(t_2)] = 0$ for $\forall t_1, t_2$ the unitary operator is calculated in the following way [25];

$$\mathcal{U}_t(t_0, t_0 + \tau) = \exp \left\{ -\frac{i}{\hbar} \int_{t_0}^{t_0 + \tau} \mathcal{H}(t) dt \right\} \quad (3.2)$$

3. Theory of measuring power line induced transition frequency shifts with a qubit

with the initial time t_0 and the period of time evolution τ . Using the properties of Pauli-matrices the operator is given by

$$\mathcal{U}_t(t_0, t_0 + \tau) = \begin{pmatrix} \exp\left\{-\frac{i}{2}\phi\right\} & 0 \\ 0 & \exp\left\{\frac{i}{2}\phi\right\} \end{pmatrix}, \quad (3.3)$$

which corresponds to a rotation around σ_z on the Bloch sphere with a rotation angle equal to the accumulated phase $\phi = \int_{t_0}^{t_0+\tau} \Delta(t)dt$.

To show how the magnetic field noise affects the qubit state, a superposition state is considered. Because the initial phase of the superposition state can be arbitrary, the chosen state is $|+\rangle_y = \frac{|\uparrow\rangle + i|\downarrow\rangle}{\sqrt{2}}$. The noise changes the phase of the state by the accumulated phase ϕ during the time evolution

$$|+\rangle_y = \frac{1}{\sqrt{2}} (|\uparrow\rangle + i|\downarrow\rangle) \xrightarrow{\mathcal{U}_t} \frac{1}{\sqrt{2}} (|\uparrow\rangle + ie^{i\phi}|\downarrow\rangle), \quad (3.4)$$

hence the name dephasing noise.

In order to observe this behavior in an experiment, where the qubit is measured being in the excited state $|\uparrow\rangle$ or in the ground state, the superposition state is created by applying a $\frac{\pi}{2}$ -pulse on the ground state $|\downarrow\rangle$. During the time evolution τ the state precesses in the equatorial plane for a non zero noise $\Delta(t) \neq 0$ and dephases if $\Delta(t)$ contains random fluctuations. The second $\frac{\pi}{2}$ -pulse maps the state back to the measurement basis. This is the so called *Ramsey* experiment. The corresponding pulse sequence is illustrated in figure 3.1. The probability of measuring the qubit in the excited state, when the ion is initially in the ground state, is

$$\begin{aligned} P_\uparrow &= |\langle \uparrow | \mathcal{U}_R\left(\frac{\pi}{2}, \varphi_l\right) \mathcal{U}_t(t_0, t_0 + \tau) \mathcal{U}_R\left(\frac{\pi}{2}, 0\right) |\downarrow\rangle|^2 \\ &= \frac{1}{2} + \frac{1}{2} \cos(\phi + \varphi_l) \end{aligned} \quad (3.5)$$

The phase $\omega t_0 + \beta$ can now be seen as a relative phase between the noise and the Ramsey experiment. The probability oscillates with varying period τ or starting time t_0 . In our experiment we are able to shift the pulse sequence with respect to the noise. This is possible, because the experiment is line-triggered by the AC mains and the experiment start can be delayed from the trigger point. The noise is created by the AC mains so delaying the experiment start referred to the trigger corresponds to delaying the experiment start to the noise. In the formula this is reflected in a change of the starting time t_0 . Performing Ramsey experiments by delaying the starting time t_0 with respect to the line-trigger over one total cycle of the 50 Hz AC mains (20 ms) is what we call a line cycle measurement. By setting the laser phase of the second $\frac{\pi}{2}$ -pulse to $\varphi_l = \frac{\pi}{2}$, the outer function of formula (3.5)

3. Theory of measuring power line induced transition frequency shifts with a qubit

becomes a sine function. The sine function is more sensitive to small variations of the argument ϕ compared to the cos function, due to its linear behavior around 0. For small variations $\max(\phi(t)) < \frac{\pi}{4}$ the sine function can be linearly approximated by $\sin(\phi) \approx \phi$ and the excitation

$$P_{\uparrow}(t_0) \approx \frac{1}{2} + \frac{\phi(t_0)}{2}$$

$$\max(P_{\uparrow}) \approx \frac{1}{2} + \frac{\Delta}{\omega} \sin\left(\frac{\omega\tau}{2}\right)$$

becomes a linear function of the magnetic field as $\Delta \sim B$.

To give an example, the case of a noise created by an oscillating magnetic field with a single frequency ω of the form $\Delta(t) = \Delta \sin(\omega t + \beta)$ is discussed. For this function, the accumulated phase is derived as

$$\phi = \int_{t_0}^{t_0+\tau} \Delta(t) dt = \frac{\Delta}{\omega} \left(\cos(\omega t_0 + \beta) - \cos(\omega t_0 + \beta + \omega\tau) \right)$$

$$= \frac{2\Delta}{\omega} \sin\left(\frac{\omega\tau}{2}\right) \sin\left(\omega t_0 + \beta + \frac{\omega\tau}{2}\right). \quad (3.6)$$

The accumulated phase reaches its maximum if the product of the noise frequency with the period of time evolution is an odd multiple of π ($\tau\omega = k\pi$ with $k = 1, 3, 5, \dots$) for a given value of $\omega t_0 + \beta$.

As we do not directly measure the accumulated phase $\phi(t_0)$ but $\sin(\phi(t_0))$ (cf. eq. (3.5)), a large noise amplitude leads to the effect of over flopping as illustrated in figure 3.2(a). In this case, the amplitude factor $\frac{2\Delta}{\omega} \sin(\omega\tau/2)$ of the accumulated phase in equation (3.6) is greater than $\frac{\pi}{2}$. The probability P_{\uparrow} is not only oscillating with the noise frequency ω but also with a component having three times the fundamental frequency shown in figure 3.2 (b) and (c). In the Bloch sphere representation the state vector is passing the x-axis during the free evolution (see figure 3.1) before the vector is mapped back to the measurement basis. This behavior makes it hard to quantify the noise with this experiment, because it is hard to distinguish between a single component noise with a high amplitude or noise with a threefold frequency component. Since the noise is produced by the ambient magnetic field in the laboratory, noise components with higher harmonics of 50 Hz also appear. Simulations of this behavior are shown in figure 3.2 (c) and (d). The formula used for the simulations is

$$P_{\uparrow} = \frac{1}{2} - \frac{1}{2} \sin \left(\sum_{j \in \{50, 150\}} \frac{2\Delta_j}{\omega_j} \sin\left(\frac{\omega_j\tau}{2}\right) \sin\left(\omega_j t_0 + \beta_j + \frac{\omega_j\tau}{2}\right) \right) \quad (3.7)$$

with the parameters for the 50 Hz and 150 Hz component as described in the caption of figure 3.2. As example for the parameters used in figure 3.2(c) the equation

3. Theory of measuring power line induced transition frequency shifts with a qubit

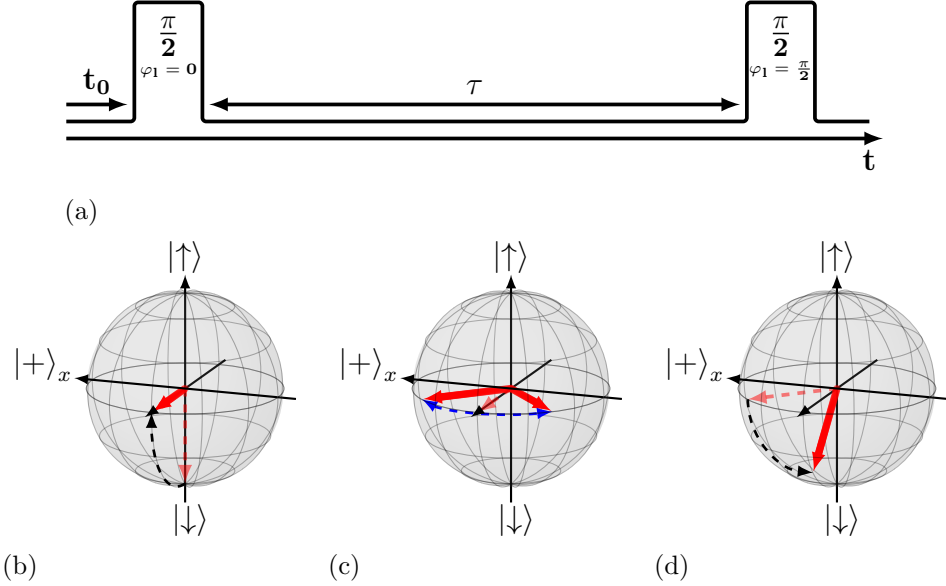


Figure 3.1.: Pulse sequence of a Ramsey experiment and state evolution on a Bloch sphere

The figure illustrates the pulse sequence (a) and the evolution of the state vector on the Bloch sphere of the Ramsey experiment. The first $\frac{\pi}{2}$ laser pulse rotates the state around x from the ground state $|\downarrow\rangle$ to the $|+\rangle_y$ state (b). The noise leads to a dephasing of the superposition state during the free evolution time τ (c). The second $\frac{\pi}{2}$ pulse with laser phase $\varphi_l = \frac{\pi}{2}$ rotates the state around y back to the measurement basis (d).

get the simplified form

$$P_{\uparrow} = \frac{1}{2} - \frac{1}{2} \sin \left(\pi \sin \left(2\pi 50 \text{ Hz} \cdot t_0 + \frac{\pi}{2} \right) \right). \quad (3.8)$$

Due to the effect of over flopping, the graph presenting a strong 50 Hz component (b) and the graph presenting two components 50 Hz and 150 Hz can only be distinguished by their curvature. Noise and measurement imperfection in the real experiment make it harder to distinguish between these two cases. A technique, described in the next section, is used that predominately senses noise of a particular frequency to overcome this problem.

3. Theory of measuring power line induced transition frequency shifts with a qubit

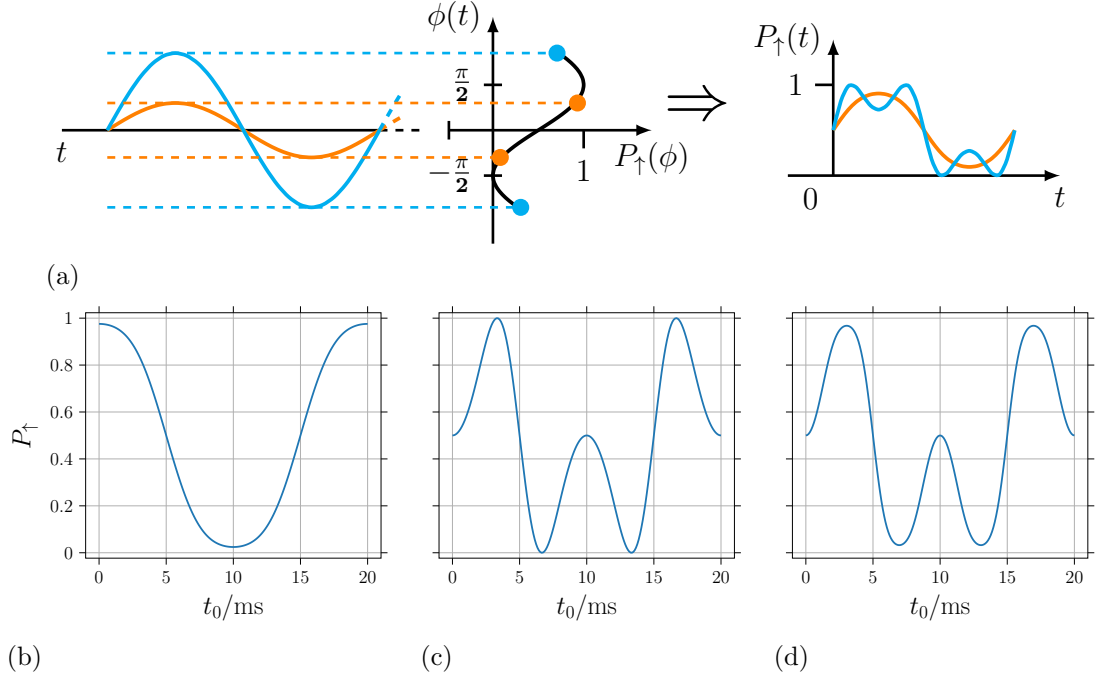


Figure 3.2.: Simulation of line cycle measurement

Panel (a) illustrates the composition of two sinusoidal functions. The inner function ϕ (orange and blue curve), which accounts for the accumulated phase during the Ramsey time, depends on the time t . The outer function P_\uparrow (black curve), which measures the Ramsey excitation, depends on the image of the inner function ϕ . One way to see the composition is, that the argument of the outer function does not change linear (left graph in (a)), but is oscillating between the maxima and minima of the inner function (blue or orange dashed lines). In the orange case the amplitude of the inner function is smaller than $\pi/2$. The corresponding outer function is not reaching its maximum, but is oscillating between the orange points. This leads to a composite function $P_\uparrow(t)$, drawn in orange in the right graph of (a), with reduced amplitude. In case the amplitude of the inner function is bigger than $\pi/2$, which is drawn in blue, the outer function is passing its maximum and oscillates between the two blue points. The corresponding composite function $P_\uparrow(t)$ in the right graph of (a) is reaching its maximum and folds back in. This effect is called over flopping in this work. The lower graphs show simulations of the line cycle measurement based on equation (3.7) to illustrate the mechanism of over flopping. In all three graphs, a noise frequency of 50 Hz is present with amplitudes of $\Delta_{50} = 0.8 \cdot \omega_{50}\pi/4$ (b), $\Delta_{50} = 2 \cdot \omega_{50}\pi/4$ (c) and $\Delta_{50} = 0.5 \cdot \omega_{50}\pi/4$ (d). In graph (d) a noise component with threefold the frequency 150 Hz and amplitude $\Delta_{150} = 0.5 \cdot \omega_{150}\pi/4$ is added. The period τ is chosen to $\tau = \pi/\omega_{50} = 10$ ms.

3. Theory of measuring power line induced transition frequency shifts with a qubit

3.2. π -pulse train and the CPMG sequence

Imperfectly isolated quantum systems couple to the environment, which can lead to decoherence and dephasing. In nuclear magnetic resonance experiments, sequences with multiple π -pulses were used for fighting decoherence [30]. These sequences are generalizations of spin-echo experiments (also called Hahn echo) [31]. The method of applying periodic pulses to decouple the qubit from the environment to suppress decoherence, is called Dynamical Decoupling [32, 33]. In reference [34, 35], the usage of multipulse sequences was extended to analyse the noise spectrum.

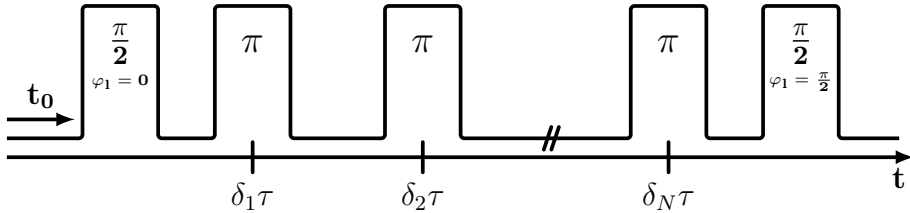


Figure 3.3.: π -pulse train

The diagram illustrates the pulse sequence of a π -pulse train with N π -pulses embedded in a Ramsey sequence. The overall duration of the sequence is τ . The normalized position δ_j of the j^{th} π -pulse is a real number between $\delta_0 = 0$ and $\delta_{N+1} = 1$. The center of the j^{th} π -pulse occurs at the time $\delta_j\tau$. Similar to the case of the Ramsey experiment, t_0 describes the time delay from the line-trigger of the sequence.

Similar to the description in the section before the accumulated phase is

$$\phi = \int_{t_0}^{t_0+\tau} \mathcal{F}(t)\Delta(t)dt, \quad (3.9)$$

where a filter function $\mathcal{F}(t)$ is mathematically representing the π -pulse sequence at the starting point t_0 of the experiment [35]. In the time domain, the filter function can be written as a function

$$\mathcal{F}(t) = \begin{cases} 0, & t < 0 \\ (-1)^j, & \delta_j\tau \leq t < \delta_{j+1}\tau \text{ between } \pi\text{-pulses} \\ 0, & t \geq \tau \end{cases} \quad (3.10)$$

alternating between ± 1 between the interpulse free evolution periods. In the frequency domain, the filter function has the form

$$\tilde{\mathcal{F}}(\omega) = \frac{1}{\sqrt{2\pi i\omega}} \left[1 + (-1)^{N+1}e^{i\omega\tau} + 2 \sum_{j=1}^N (-1)^j e^{i\omega\tau\delta_j} \right] \quad (3.11)$$

3. Theory of measuring power line induced transition frequency shifts with a qubit

with the overall sequence duration τ , the number of pulses N and, as shown in figure 3.3, the occurrence of the j^{th} pulse at time $\delta_j\tau$ [36]. In this formula the length of π -pulses is negligible, which approximates the situation in our experiment, where the length of a π -pulse is in the order of $\approx 5\mu\text{s}$ compared to the sequence length $\tau = 20\text{ ms}$. The individual phases of the π -pulses do not influence the filter function, but add a phase to the accumulated phase ϕ . For more details on the influence of the phase of the π -pulses and a precise derivation of the filter function see Appendix A.

A special case of the spin echo sequence, where the pulses are all equidistant, is the CPMG sequence (after Carr, Purcell, Meiboom and Gill)[16]. As illustrated in figure 3.4(a) the time distance to the embedding $\frac{\pi}{2}$ -pulses is half the interpulse distance. This pulse spacing is mathematically written as $\delta_j = \frac{j-\frac{1}{2}}{N}$ in formula (3.11). The filter function for different numbers of π -pulses is plotted in figure 3.5. From the graphs one can see that the maximum of the filter function - or in other words the frequency component where the CPMG sequence is most sensitive to - occurs at a frequency $f_{max} \approx \frac{N}{2\tau}$. Smaller local maxima occur for odd multiples of f_{max} . Signals with frequencies $f = \frac{k}{\tau}$ for even numbers of pulses and $f = \frac{k}{\tau} + \frac{1}{2\tau}$ for odd numbers of pulses are suppressed, except f_{max} and its odd multiples. The accumulated phase (3.9) can be written in the frequency domain

$$\phi = \int_{-\infty}^{\infty} \tilde{\mathcal{F}}(\omega) \tilde{\Delta}^*(\omega) e^{i\omega t_0} d\omega, \quad (3.12)$$

for details see appendix A. The noise with discrete frequency components f_j is represented by delta functions in the frequency domain

$$\begin{aligned} \Delta(t) &= \sum_j \Delta_j \sin(\omega_j t + \beta_j) \\ \tilde{\Delta}(\omega) &= \sum_j \frac{\sqrt{2\pi}}{2i} \Delta_j (e^{i\beta_j} \delta(\omega - \omega_j) - e^{-i\beta_j} \delta(\omega + \omega_j)). \end{aligned}$$

Substituting this in equation (3.12) and carrying out the integration gives the phase

$$\phi = \sum_j \sqrt{2\pi} \Delta_j |\tilde{\mathcal{F}}(\omega_j)| \sin(\omega_j t_0 + \beta_j + \arg(\tilde{\mathcal{F}}(\omega_j))) \quad (3.13)$$

with the absolute value of the filter function $|\tilde{\mathcal{F}}(\omega_j)|$ and the phase of the filter function $\arg(\tilde{\mathcal{F}}(\omega_j))$. A precise derivation is presented in appendix A. Similar to the line cycle measurement, the CPMG sequence is delayed with respect to the line-trigger, in order to quantify the noise parameters Δ_j and b_j . The number N of pulses and the sequence length are chosen in such a way that the measurement

3. Theory of measuring power line induced transition frequency shifts with a qubit

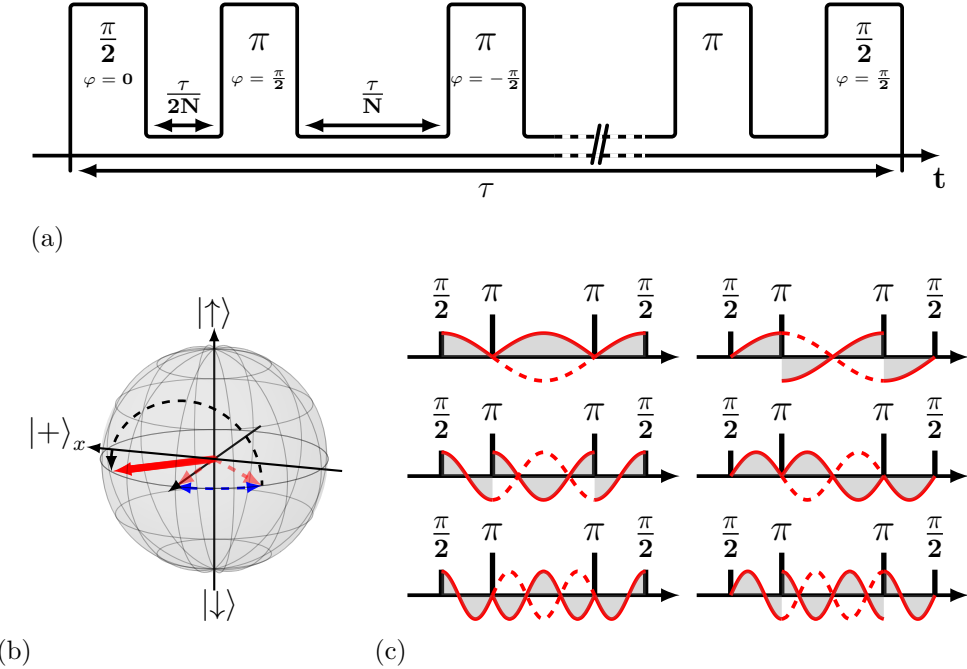


Figure 3.4.: CPMG sequence

The CPMG sequence with N pulses and an overall sequence length τ is illustrated in (a). The π -pulses with alternating laser phase $\varphi_l = \pm\frac{\pi}{2}$ are equidistant with $\frac{\tau}{N}$. The distance to the embedding $\frac{\pi}{2}$ -pulses is half of the interpulse distance. The effect of a π -pulse to the state vector is illustrated on the Bloch sphere in (b). The π -pulse rotates the state vector half around the y-axis. The right diagram (c) illustrates the mechanism of the CPMG sequence in another way of seeing the effect of π -pulses. The π -pulse flips the sign of the oscillating noise, which is drawn as red sinusoidal curve (compared to the dashed red line). The accumulated phase ϕ is the integral over the curve, illustrated as gray areas. For the frequency $f_1 = \frac{N}{2\tau} = \frac{1}{\tau}$ the accumulated phase is maximum (upper left graph in (c)) or zero (upper right graph in (c)), depending on the phase relation between the noise and the CPMG sequence. For a noise with twice the frequency $f_2 = 2f_1$ the accumulated phase is zero, independent of the phase relation between noise and sequence. Depending on the phase relation a threefold frequency $f_3 = 3f_1$ noise (lower graphs in (c)) can have a non zero accumulated phase, which is, however, smaller than the accumulated phase of the fundamental frequency.

is most sensitive to the frequency of interest. In order to sense the AC mains magnetic field with the main component of 50 Hz, a sequence length of $\tau = 20$ ms with two π -pulses is chosen. The corresponding filter function is shown in figure 3.5(a). Even numbers of π -pulses are then used to measure the higher harmonics of 50 Hz, for example $N = 6$ pulses to measure 150 Hz. Using even numbers of pulses allows us to apply pulses with alternating laser phases $\varphi_l = \pm\frac{\pi}{2}$, so

3. Theory of measuring power line induced transition frequency shifts with a qubit

that the state vector on the Bloch sphere 3.4(b) is rotating around the same axis back and forth. This method overcomes the problem of imperfect π -pulses, where the vector is not fully rotated back into the x-y-plane. By rotating back by the same amount, the second pulse places the state vector back into the x-y-plane. In order to get the probability P_\uparrow the accumulated phase (3.13) is substituted into formula (3.5). Simulations of CPMG scans with frequency components 50 Hz and 150 Hz are shown in figure 3.6. For strong magnetic fields, the measured probability exhibits the same over flopping features as the Ramsey experiment. In the simulated measurement, to sense the 50 Hz component 3.6(b), the 150 Hz component is still present, which leads to a shift of the over flopping dips. In the simulation sensing the higher frequency component 3.6(c) the 50 Hz component is suppressed (see also filter function 3.5 (b) and (c)), which allows a more precise analysis of this component.

Assuming a CPMG sequence with $N = 0$ pulses (Ramsey experiment) the absolute value of the filter function (3.11) is $|\tilde{\mathcal{F}}| = \frac{2}{\sqrt{2\pi}\omega} \sin\left(\frac{\omega\tau}{2}\right)$ and the argument is $\arg(\tilde{\mathcal{F}}) = \frac{\omega\tau}{2}$.¹ In this way, equation (3.13) can be linked to equation (3.6).

¹Precisely the absolute value is $|\tilde{\mathcal{F}}| = \left|\frac{2}{\sqrt{2\pi}\omega} \sin\left(\frac{\omega\tau}{2}\right)\right|$ and the argument is $\arg(\tilde{\mathcal{F}}) = \frac{\omega\tau}{2}(+\pi)$ with additional π shift for all values with $\sin\left(\frac{\omega\tau}{2}\right) < 0$. This alternating π shift leads to a sign change of the sin function in eq. (3.13), which gives the same result as setting $|\tilde{\mathcal{F}}| = \frac{2}{\sqrt{2\pi}\omega} \sin\left(\frac{\omega\tau}{2}\right)$ without an alternating π shift.

3. Theory of measuring power line induced transition frequency shifts with a qubit

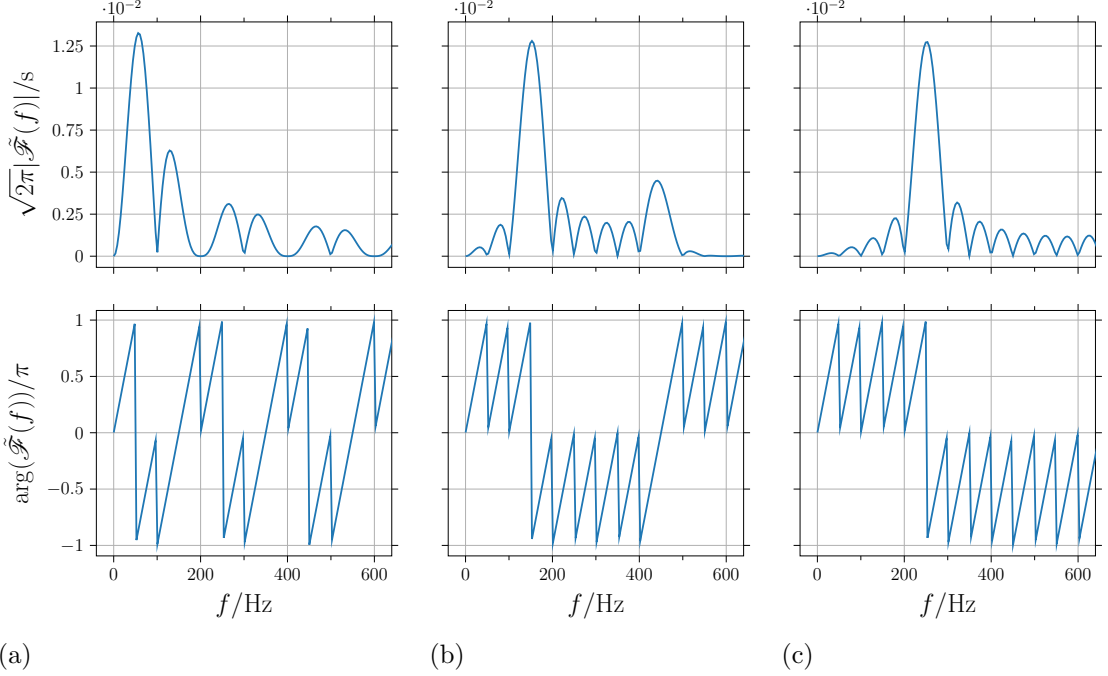


Figure 3.5.: Filter function

The graphs show the absolute value and the argument of the filter function (3.11) of CPMG sequences with various numbers of pulses depending on the frequency. For a fixed length $\tau = 20 \text{ ms}$ graph (a) shows the filter function with $N = 2$ pulses, (b) with $N = 6$ and (c) $N = 10$.

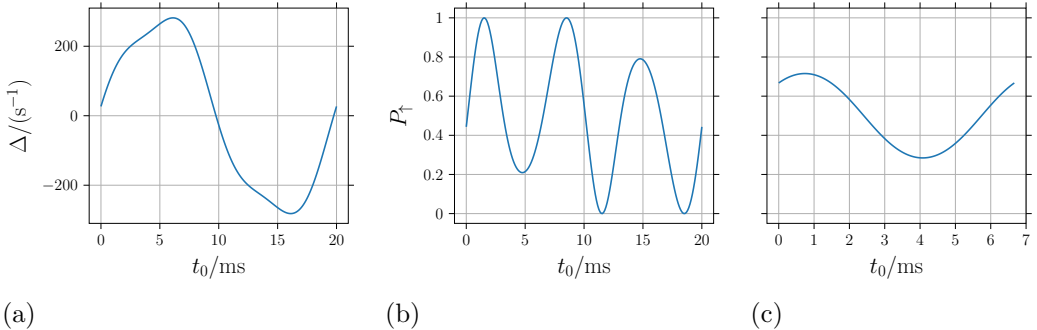


Figure 3.6.: Simulation of a CPMG scan

The left graph (a) shows the time trace of the noise with a 50 Hz and 150 Hz modulation. The parameters are $\Delta_{50} = 287 \text{ s}^{-1}$, $\beta_{50} = 0$ and $\Delta_{150} = 35 \text{ s}^{-1}$, $\beta_{150} = 50^\circ$. The right graphs show the CPMG scans with $N = 2$ (b) and $N = 6$ (c) pulses and a length $\tau = 20 \text{ ms}$ based on formula (3.5) and (3.13).

3. Theory of measuring power line induced transition frequency shifts with a qubit

3.3. Asynchronous noise

Whereas the two previous sections dealt with experiments that are synchronised to the fundamental frequency at which noise occurs, this section discusses the case of an asynchronous noise. In other words the CPMG sequence and the noise are not synchronous and the phase relation $\omega_j t_0 + \beta_j$ is arbitrary. Because each point of a measurement is the average of multiple quantum projection measurements, the equation for the excitation (3.5) becomes

$$\langle P_{\uparrow} \rangle = \frac{1}{2} + \frac{1}{2} \langle \cos(\phi + \varphi_l) \rangle, \quad (3.14)$$

where the probability is averaged over the varying starting time t_0 [35]. With the help of the angle-sum identity for trigonometric functions the probability is

$$\langle P_{\uparrow} \rangle = \frac{1}{2} + \frac{\langle \cos(\phi) \rangle}{2} \cos(\varphi_l). \quad (3.15)$$

The sin part is neglected in the formula, because the symmetry of the sin function and the periodicity of the accumulated phase ϕ leads to an average of $\langle \sin(\phi) \rangle = 0$. As illustrated in figure 3.7 varying the laser phase φ_l leads to contrast fringes with an amplitude $C = \langle \cos(\phi) \rangle$.² The average over the starting time t_0 with the period T is

$$\begin{aligned} \langle \cos(\phi) \rangle &= \frac{1}{T} \int_0^T \cos(\phi(t_0)) dt_0 \\ &= \frac{1}{T} \int_0^T \cos \left(\sum_j \sqrt{2\pi} \Delta_j |\tilde{\mathcal{F}}(\omega_j)| \sin(\omega_j t_0 + \beta_j + \arg(\tilde{\mathcal{F}}(\omega_j))) \right) dt_0 \end{aligned} \quad (3.16)$$

with the accumulated phase $\phi(t_0)$ from equation (3.13). This equation can only be solved analytically for a single noise component.

In the Bloch sphere picture the non-synchronicity leads to multiple different dephased states as illustrated in figure 3.7 (b). Averaging over these multiple states corresponds to a state vector with reduced length. The maximum and minimum of the contrast fringes are equal to the length of the averaged state vector.

²In this work a positive amplitude $C = |\langle \cos(\phi) \rangle|$ is used. Because the contrast can also have negative values, an additional phase parameter b in $\cos(\varphi_l + b)$ is used for the analysis.

3. Theory of measuring power line induced transition frequency shifts with a qubit

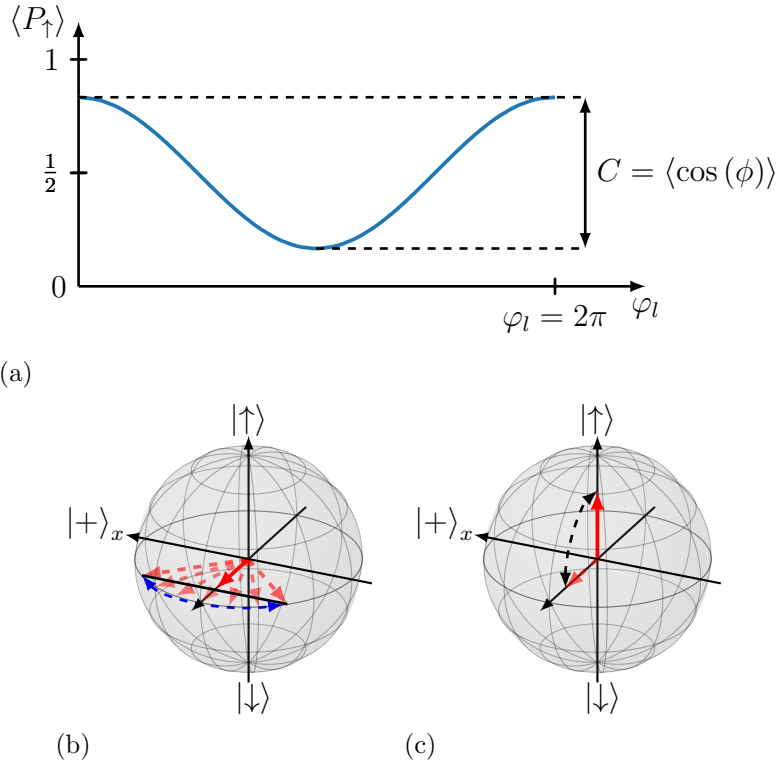


Figure 3.7.: Contrast fringes

The graph illustrates the contrast fringes by scanning over the laser phase φ_l . The measurement is performed by averaging over multiple quantum projection measurements $\langle P_{\uparrow} \rangle$. Asynchronous noise leads to a decrease of the contrast C . Figure (b) and (c) illustrate the loss of contrast on the Bloch sphere. Multiple dephased state vectors are drawn with red dashed arrows. Averaging over these states leads to a state vector with reduced length, which is drawn as black line. The reduced state is then mapped back to the measurement basis.

4. Experimental setup

The first part of this chapter gives an overview of the experimental setup of the QSIM experiment and the Precision experiment and additionally presents the already existing components for suppressing the magnetic field noise in the experiments. After that, the components of the feed-forward compensation system are described.

4.1. Ion trap setup

A drawing of the vacuum chamber of the QSIM experimental setup is presented in figure 5.8. The illustration shows the geometry of directions that are available for sending laser beams into the vacuum chamber. The magnetic field for the quantization axis is created by permanent magnets. The permanent magnets are made of $\text{Sm}_2\text{Co}_{17}$. The two pairs of magnetic field coils, which are used for fine tuning of the magnetic field and compensating the magnetic field gradient as well as for the magnetic field noise compensation, are drawn in orange. The setup of the precision experiment is shown in figure 4.2(a). There are magnetic field coils on the top and bottom ports, the left and right ports as well as the back and front of the chamber in figure 4.2. In the Precision setup the magnetic field of the quantization axis is also created by permanent magnets.

In both experimental setups, there are already components available for suppressing magnetic field noise: A mu-metal shielding surrounding the vacuum chamber and a line trigger for synchronizing the experiment cycle with the AC mains phase. There are several small holes in the shielding (see the backside and right in figure 4.2(a) and the right in figure 4.2(b)) to provide access to the chamber for optical fibers and electronic cables [18, 37]. Due to power cables running into the shielding the AC magnetic field noise is still present in the vacuum chamber. Using the line trigger, the ions experience the same magnetic field modulation in every experimental cycle. As a result, the AC mains induced magnetic field noise is not a random fluctuation of the ions transition frequency anymore but a constant modulation of the transition frequency (refer to section 3.3). But during one period of the AC mains the transition frequency is modulated depending on the strength of the magnetic field. To suppress this modulation and even be able to not use the line trigger anymore, a feed-forward compensation system is installed

4. Experimental setup

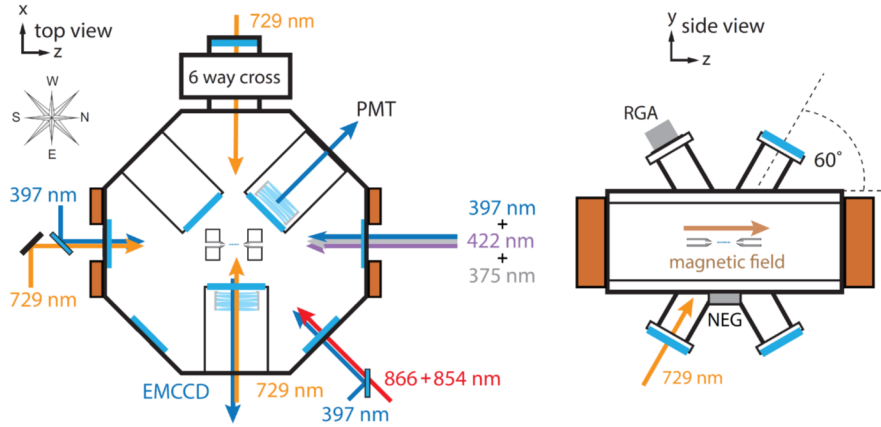


Figure 4.1.: QSIM chamber with laser directions

The illustrations show a top and side view of the vacuum chamber and the ion trap drawn in the center. The arrows show the access of the different laser beams into the chamber. The orange rectangle illustrates the magnetic field coils. The laser beams used for the Raman transition are not shown in the drawing. In the side view they access the chamber from the top right port. The read out is done via the photo multiplier (PMT) and the camera (EMCCD).

at both experiments.

4. Experimental setup

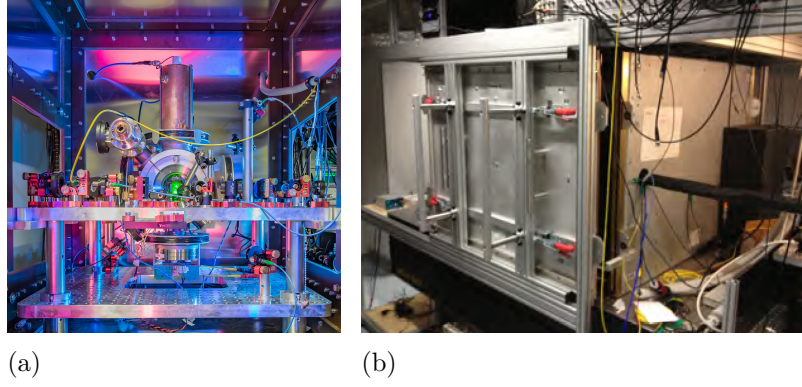


Figure 4.2.: Photos of QSIM and Precision setup

Figure (a) shows a picture of the vacuum chamber of the Precision experiment inside the mu-metal shielding. Figure (b) shows the mu-metal shielding covering the vacuum chamber of the QSIM experiment. Photo (b) is taken from [18].

4.2. Feed-forward system for noise cancellation

The compensating system contains the magnetic field coils of the trap and a function generator to modulate the magnetic field at the coils. As function generator a programmable RedPitaya STEMLab board, which is described in detail in the second subsection, is used.

4.2.1. Characterisation of the coil system

There are two sets of magnetic field coils attached to the chamber (see figure 4.1). The inner coils are used in DC for compensating the remaining magnetic field gradient from the permanent magnets. The outer coil set is used for the magnetic field noise compensation system. The geometry of the magnetic field coils is shown in figure 4.3 and the physical parameters of the coils are presented in table 4.1. The DC magnetic field created by the coils is shown in figure 4.4. The magnetic strength is measured by applying a $I = 180\text{ mA}$ DC current to the coils and scanning the magnetic field at different points between the coil pairs with a fluxgate magnetometer. From this figure it can be extracted that a current of $I = 180\text{ mA}$ changes the magnetic field half-way between the coils by approximately $B \approx 180\text{ mG}$. It is necessary to mention that the measurement was taken with the coils alone and not attached to the chamber, hence this value does not give a precise magnetic field at the ions in the trap. But this is not a big problem because a precise magnetic field is not needed for the compensation routine described in chapter 5.1.1 and the value can be used as orientation and starting point.

The coil system of the Precision experiment is different. Only a single pair of

4. Experimental setup

Table 4.1.: Coil properties of the magnetic field coils in the QSIM experiment

Winding per coil N	130
Resistance per coil R/Ω	1.3
Inductance two coils connected L/mH	3

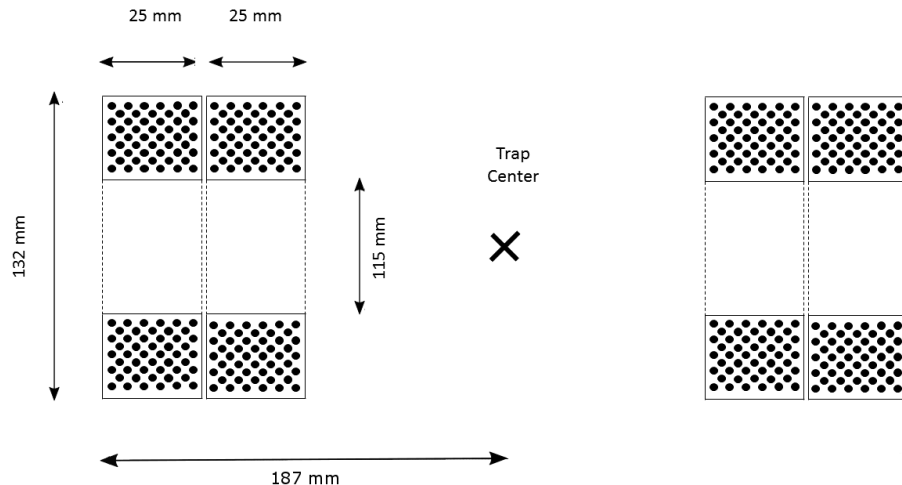


Figure 4.3.: Magnetic field coils geometry

The illustration shows the geometric structure of the magnet field coils. The inner coils are used for the magnetic field gradient compensation and the outer ones for the magnetic field noise compensation.

magnetic field coils is attached to the chamber. The coils deliver a magnetic field strength of $B \approx 5 \text{ mG}$ for a DC current of $I = 1 \text{ mA}$. This value is also used as starting point for the compensation routine. In both experiments the coils along the quantization axis are used.

4. Experimental setup

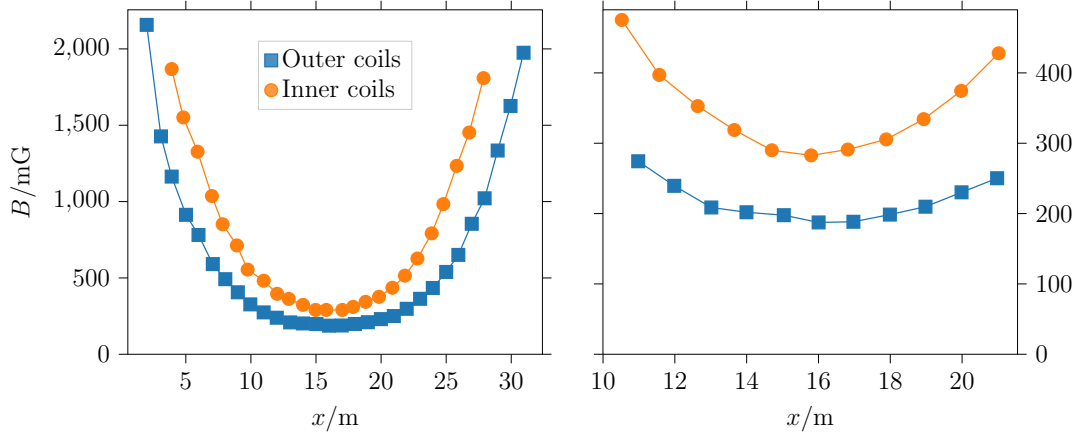


Figure 4.4.: B-field of coils The graphs show the magnetic field of the two coil pairs for an applied DC of $I = 180$ mA. Graph (b) shows a closer look.

4.2.2. Function generator system

As programmable function generator a RedPitaya STEMLab board 125-14 is used. It has two fast analogue outputs with a sample rate of 125 MS/s and a digital-to-analog converter resolution of 14 bit. The output voltage range is limited to ± 1 V with an output load 50Ω . The communication between the laboratory PC and the RedPitaya is done via LAN connection and the local network of the laboratory. The user interface of the operating system of the RedPitaya (see figure 4.6(a)) can then be accessed via the PCs browser. The board is programmed by the RedPitaya SCPI (Standard Commands for Programmable Instrumentation) commands.¹ For a simple operation of the system a controlling software, a stand-alone program based on a python program, including an user interface (see figure 4.6(b)), was developed. The software translates the actions on the user interface into a string of SCPI commands and sends it to the RedPitaya. The controlling software includes a manual operation mode and automated fit mode. The manual mode allows to set the parameters frequencies (in Hz), amplitudes (in mV) and phases (in deg), as well as the DC offset of multiple sinusoidal signals, whose superposition is then applied with the RedPitaya. Additionally it is possible to choose the trigger of the signal between internal (INT) and an external source (EXT_PE or EXT_NE). The parameters can be saved in a txt file or loaded from that one. For more details of the programming of the controlling software and the automated fit mode see appendix B. On the hardware side the RedPitaya board is connected to the line trigger via a voltage divider as shown in figure 4.6(c). This is necessary, so that the

¹For details on the connection of the RedPitaya SCPI server see the Labblogs.quantumoptics QuQIS or [38]

4. Experimental setup

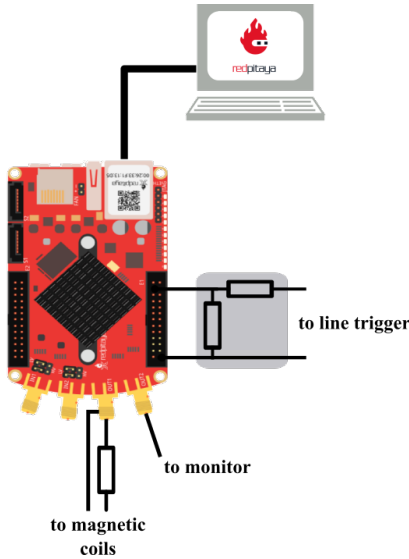
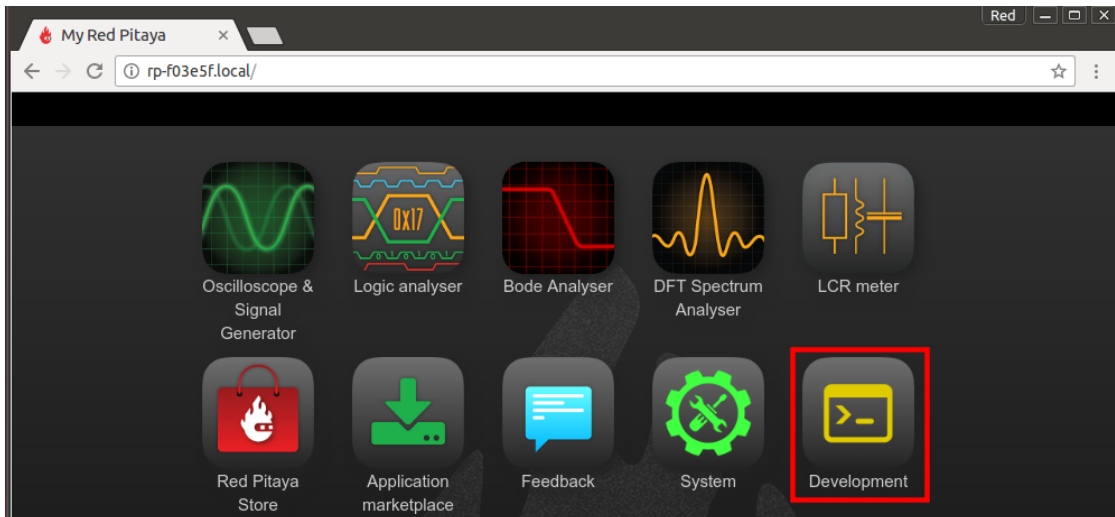


Figure 4.5.: Hardware of feed-forward system for noise cancellation

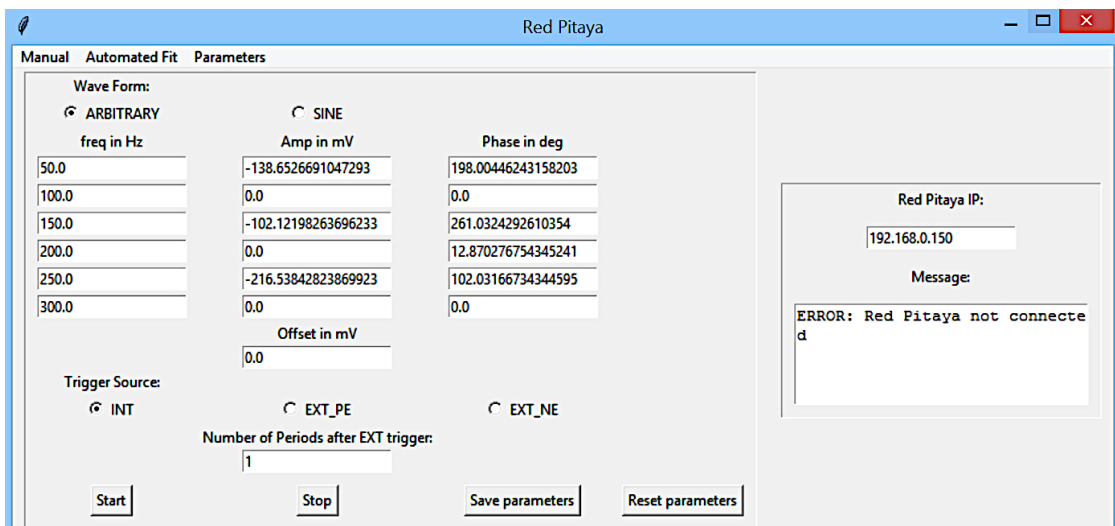
The illustration shows the connections to the RedPitaya board. The magnetic field coils are connected to the first fast analogue output of the board. The second analogue output is used for observing the compensation signal on an oscilloscope. The board is connected to the line trigger with a voltage divider placed in front. It is connected to the local network of the laboratory, where it can be operated from the laboratory PC.

compensation signal is synchronised to the AC mains and its phase position does not drift to the magnetic field noise. The RedPitaya requires a 3.3 V trigger signal. Therefore the 5 V trigger signal from the line trigger is converted to a 3.3 V signal with a voltage divider. For the voltage divider one resistor of $3.3\text{ k}\Omega$ is connected in parallel with the line trigger output and a $2.7\text{ k}\Omega$ resistor is connected in series. The first analogue output is connected to the magnetic field coils including a resistor in series. This resistor is used for termination and also as gain factor. In the QSIM experiment a resistor of $4.7\text{ k}\Omega$ is used and in the Precision experiment a resistor of $11.2\text{ k}\Omega$. An applied amplitude of 100 mV DC then leads to a magnetic field of $B \approx 21\text{ }\mu\text{G}$ in the QSIM setup or $B \approx 45\text{ }\mu\text{G}$ in the Precision setup. The second analogue output is used to monitor the applied compensation signal at an oscilloscope.

4. Experimental setup



(a)



(b)

Figure 4.6.: Software of feed-forward system for noise cancellation

Picture (a) shows the user interface of the RedPitaya operating system. The second picture (b) shows the graphical user interface for the control software of the feed-forward compensation system. For details of the control software see appendix B.

5. Experimental compensation of magnetic field noise

This chapter presents the experimental results of the compensation of line synchronous modulation of the transition frequency with the feed-forward system described in the section before. The chapter is separated in two parts, first the results from the work at the QSIM experiment is presented and in the second part the compensation at the Precision experiment is shown.

5.1. Compensation of magnetic field noise at the QSIM experiment

The section presenting the results from the QSIM experiment is structured in the following way: At first, the results of noise analysis and compensation using the Raman transition with a semi-automatic iterative routine, which was developed in the later stage of the master project, are presented. Additionally the day to day variations of the noise parameters are shown. The second part shows the analysis and compensation using the 729-transition.

5.1.1. Characterisation of noise components with the Raman transition

As described in chapter 3.2 the noise is characterised with the help of a CPMG sequence scanned over a line cycle by increasing the duration of the Doppler cooling stage, which precedes the CPMG sequence pulses from 3 ms to 23 ms. The temporal sequence of laser pulses used in the experimental sequence is shown in figure 5.1. The time delay from the start of the experiment (including laser cooling and state preparation) to the actual start of the CPMG sequence is called t_0 . For a total CPMG sequence length of $\tau = 20$ ms, the number of π -pulses N is then chosen to be most sensitive to the modulation with $f = 50$ Hz ($N = 2$) and higher odd harmonics $f = 150$ Hz ($N = 6$) and $f = 250$ Hz ($N = 10$). The even higher harmonics were also measured, but not actively cancelled, because the component are already very small (see 5.3). In the following, a semi-automatic iterative

5. Experimental compensation of magnetic field noise

routine is presented by taking the example of analysis and compensation of the $f = 250$ Hz noise component, using a CPMG sequence with length $\tau = 20$ ms and $N = 10$ π -pulses.

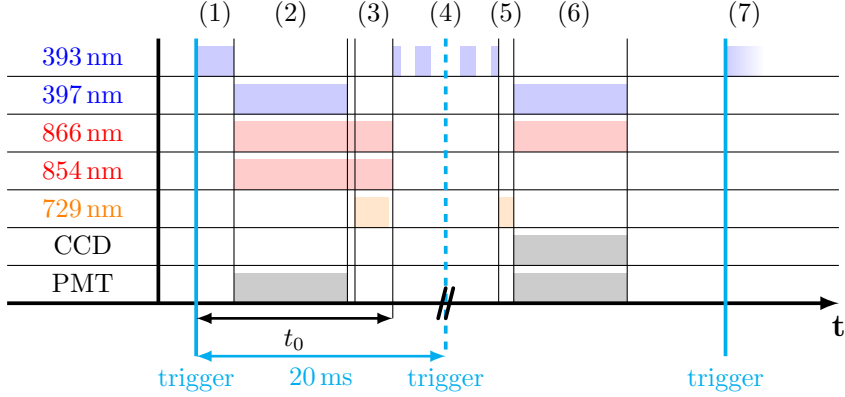


Figure 5.1.: Raman experiment sequence

The diagram shows the laser sequence for an experiment using the Raman transition. The single steps and their length are: (1) Intensity stabilisation (~ 0.5 ms), (2) Doppler cooling (3 ms to 23 ms), (3) state preparation (~ 0.1 ms), (4) measurement sequence (20 ms), (5) state mapping ($\sim 5 \mu$ s), (6) state detection (5 ms), (7) next measurement. t_0 is the delay from the line trigger to the start of the measurement sequence. The state mapping maps the $|4^2S_{1/2}, m = 1/2\rangle$ state to the $|3^2D_{5/2}, m = 5/2\rangle$, so that the state detection is similar to the one used in experiments with the optical qubit.

The noise parameters A (in s^{-1}) and ϕ_{noise} are obtained from fitting the measurement data with the modified version of formula (3.13) and (3.5)

$$P_\uparrow = \frac{1}{2} + \frac{C}{2} \sin \left(|\tilde{\mathcal{F}}(f; N, \tau)| \cdot A \sin \left(2\pi f t_0 + \phi_{\text{noise}} + \arg(\tilde{\mathcal{F}}(f; N, \tau)) \right) \right) \quad (5.1)$$

with an overall contrast C of the signal. For simplification only one frequency f is fitted, assuming the higher frequency components are small. The contributions of 250 Hz and 150 Hz are not fully suppressed by the CPMG sequence detecting the 50 Hz component (see filter function 3.5). To make sure that these components do not distort the measurement of the 50 Hz component, the higher noise frequencies 250 Hz and 150 Hz have to be compensated first. Because the overall contrast C in equation (5.1) has an influence on the fit parameter A , the contrast is obtained by scanning over the laser phase of the last $\frac{\pi}{2}$ -pulse of the CPMG sequence and fitting these contrast fringes with equation

$$P_\uparrow = \frac{1}{2} + \frac{C}{2} \cos(\varphi_l) \quad (5.2)$$

5. Experimental compensation of magnetic field noise

(refer to the contrast fringe in section 3.3). The corresponding measurement result for the noise component of 250 Hz is shown in figure 5.2(a). This overall contrast reduction can be explained by line-asynchronous noise as described in section 3.3. In the experiments with the Raman transition, the contrast does not show an dependence on the number of π -pulses. So is the contrast of a measurement with $N = 2$ pulses $C = 0.93(2)$, for a measurement with $N = 6$ pulses $C = 0.92(2)$ and for $N = 10$ pulses $C = 0.93(2)$. After having determined the contrast, the first CPMG scan to analyse the noise parameters is performed and fitted with equation (5.1). The results are shown in figure 5.2(b). The amplitude, which can be applied with the RedPitaya, is calculated from the amplitude we get from the fit by

$$A[\text{V}] = \frac{A[\text{s}^{-1}]}{\gamma \cdot 2\pi \cdot 1.399 \text{ s}^{-1}/\mu\text{G}} k \quad (5.3)$$

with the magnetic sensitivity γ of the used transition and the scaling factor k . The scaling factor is the ratio between the termination resistor and the ratio between the coil current and the magnetic field. The factor for the QSIM setup is $k = 4700 \text{ V/G}$. The obtained amplitude and phase are applied to the feed-forward system. The reaming modulation is shown in figure 5.2. The electronic filter behavior of the feed-forward system can lead to a reduction of the amplitude as well as to an additional phase shift ϕ_{shift} of the applied signal. This amplitude reduction can be denoted by a scaling factor a . If the noise and the applied compensation signal do not perfectly cancel each other out, their superposition leads to a remaining part

$$A_{noise} \sin(2\pi ft + \phi_{noise}) + \underbrace{a \cdot A_{applied}}_{A_{measured}} \sin(\underbrace{2\pi ft + \phi_{applied} + \phi_{shift}}_{\phi_{measured}}) = A_{rem} \sin(2\pi ft + \phi_{rem}), \quad (5.4)$$

which is denoted with A_{rem} and ϕ_{rem} . The signal ($A_{measured}$ and $\phi_{measured}$), which the ions actually experience, can be recalculated by rearranging equation (5.4) and with the help of the harmonic addition formula (see appendix C),

$$A_{measured} = \sqrt{A_{noise}^2 + A_{rem}^2 - 2A_{noise}A_{rem} \cos(\phi_{noise} - \phi_{rem})} \quad (5.5)$$

$$\phi_{measured} = \text{atan} 2[A_{noise} \sin(\phi_{noise}) - A_{fit} \sin(\phi_{rem}), A_{rem} \cos(\phi_{noise}) - A_{rem} \cos(\phi_{rem})]. \quad (5.6)$$

The parameters A_{noise} and ϕ_{noise} are found by fitting the initial uncompensated signal, this is shown in figure 5.2(b) and the parameters A_{rem} and ϕ_{rem} are obtained from fitting the remaining part shown in 5.2(c). The two parameters $A_{measured}$ and $\phi_{measured}$ are then calculated with formula (5.6). The amplitude reduction

5. Experimental compensation of magnetic field noise

factor a can now be obtained by dividing the calculated parameter $A_{measured}$ by the parameter $A_{applied}$, which is the known amplitude of the compensation signal applied with the RedPitaya. Analogously, the phase shift ϕ_{shift} is obtained by subtracting the phase of the compensation signal $\phi_{applied}$ from the calculated value of $\phi_{measured}$. A new amplitude for the compensation signal is calculated by dividing the measured noise amplitude by the amplitude reduction factor A_{noise}/a . The phase for the compensation signal is also updated by subtracting the phase shift ϕ_{shift} from the measured phase of the noise ϕ_{phase} . The updated parameters are used for generating a corrected compensation signal. The remaining part can be remeasured and the procedure repeated, to get more precise values for a and ϕ_{shift} . The recalculated values of the amplitude $A_{measured}$ can be fitted as a function of the applied amplitude $A_{applied}$. The slope of the linear fit gives the amplitude reduction factor a as shown in the upper graph of figure 5.2(e). The calculated values for ϕ_{shift} are averaged, which can be seen in the lower graph of figure 5.2(e). The final compensated signal is shown in figure 5.2(d). The variation of the amplitude and phase of the magnetic field components (see next section) makes a perfect suppression of the noise component impossible. Figure 5.3 shows measurements of the other relevant noise components at 50, 150, and 200 Hz. Because of the already small amplitude the even higher harmonics of 50 Hz, 100 Hz and 200 Hz are not compensated. The observed magnetic strengths of the noise amplitude, using the initially fit amplitude, are $B_{50\text{Hz}} = 28.1(2)\text{ }\mu\text{G}$, $B_{150\text{Hz}} = 13.1(3)\text{ }\mu\text{G}$ and $B_{250\text{Hz}} = 20.4(4)\text{ }\mu\text{G}$. The final remaining parts are $B_{50\text{Hz}} = 1.6(3)\text{ }\mu\text{G}$, $B_{150\text{Hz}} = 0.85(22)\text{ }\mu\text{G}$ and $B_{250\text{Hz}} = 0.56(20)\text{ }\mu\text{G}$.

5. Experimental compensation of magnetic field noise

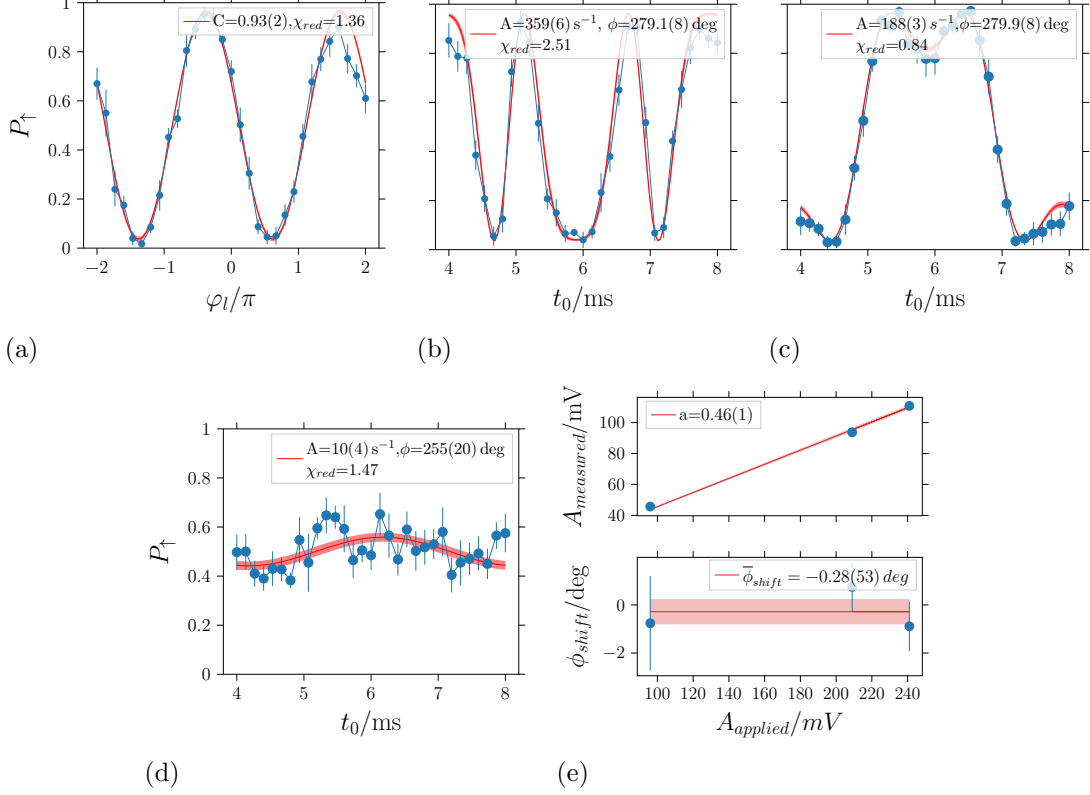


Figure 5.2.: Compensation routine

The graphs show different plots of the characterisation and compensation routine based on the example of the 250 Hz noise component. The first measurement (a) shows a scan over the laser phase of the last $\pi/2$ -pulse using a CPMG sequence with 10 π -pulses. This is used to calculate the overall contrast. The second measurement (b) is a scan of the starting time of the CPMG sequence with respect to the line cycle (short CPMG scan); this scan is used to characterize the noise parameters using formula (5.1). The gained parameters from the first fit are used for a first compensation of the noise component. Afterwards the remaining part of the noise is remeasured with the CPMG scan (c). Using the phasor addition formula (5.6) the amplitude reduction factor a and phase shift are calculated (e) and the updated parameters are used for generating a magnetic field correction $B(t)$. Repeating this procedure the amplitude factor can be calculated by linear fitting, for details see text. Graph (d) shows the compensated signal. The data points in graphs (a)-(d) are the excitation averaged over 8 ions and the error bars illustrate the corresponding standard deviations. The red bands show one sigma confidence interval of the fit parameters.

5. Experimental compensation of magnetic field noise

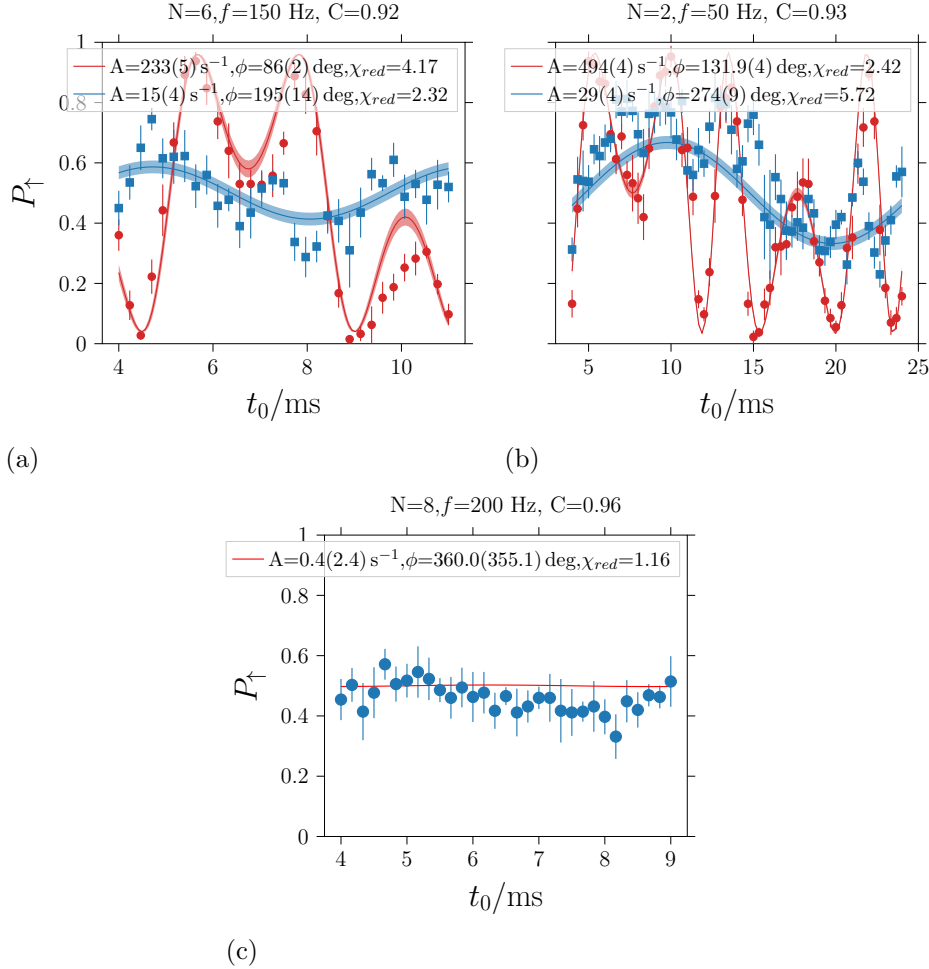


Figure 5.3.: Noise components before and after compensation by magnetic field sensing using CPMG sequences on the Raman transition

The graphs show CPMG scans over the line cycle with $N = 6$ (a), $N = 2$ (b) and $N = 8$ (c) π -pulses. The red data and fits are before compensation and the blue after compensation. The data points are the excitation averaged over 8 ions and the error bars the corresponding standard deviations. The bands show one sigma confidence interval of the fit parameters.

5. Experimental compensation of magnetic field noise

5.1.2. Noise parameter fluctuation

In order to observe the variation of the magnetic field amplitude and phase, CPMG scans from different dates and times are collected. The observed day-to-day changes of the fit amplitude and phase are shown in figure 5.4. The maximum difference in amplitude for the 50 Hz component from figure 5.4(a) is $\Delta A \approx 50 \text{ s}^{-1}$, which corresponds to a relative fluctuation of $\Delta B/B \approx 10\%$. The absolute variation of the phase is $\Delta\phi \approx 5 \text{ deg}$. For the 150 Hz (figure 5.4(a)) signal a amplitude fluctuation of $\Delta A \approx 40 \text{ s}^{-1}$ and a phase fluctuation of $\Delta\phi \approx 7 \text{ deg}$ is observed. The amplitude of the 250 Hz signal fluctuates around $\Delta A \approx 30 \text{ s}^{-1}$ and the phase $\Delta\phi \approx 5 \text{ deg}$. In summary, the amplitude of the noise fluctuates around $\Delta B/B \approx 10\%$ and the phase 5 deg, except of the 150 Hz signal, which has a bigger fluctuation of $\Delta B/B \approx 17\%$ and 7 deg.

To observe the short term fluctuation the excitation of the CPMG sequence for the compensated 50 Hz signal is observed at fixed delay times over time. This can be seen in figure 5.5. The fixed delay times are set to $t_0 = 4 \text{ ms}$ and $t_0 = 9 \text{ ms}$, which corresponds to the starting point and the maximum of the compensated signal in figure 5.3(b). The jumps and fluctuations in the signals of figure 5.5 can be explained by the amplitude fluctuation of the 50 Hz noise. As described before the amplitude fluctuates by $\Delta A \approx 50 \text{ s}^{-1}$, using the harmonic additions formula, this is reflected in a similar amplitude fluctuation for the remaining part. The amplitude variation leads to the fluctuation of the probability at the maximum point $t_0 = 9 \text{ ms}$ between ~ 0.3 and ~ 0.8 and at the starting point $t_0 = 4 \text{ ms}$ between ~ 0.2 and ~ 0.7 .

5. Experimental compensation of magnetic field noise

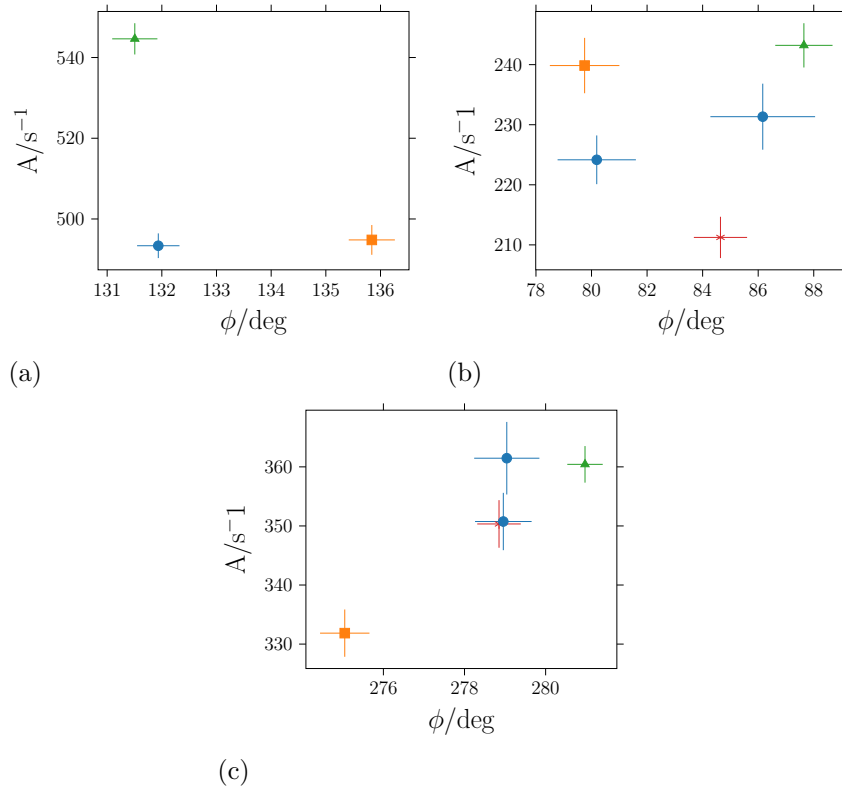


Figure 5.4.: Noise parameter fluctuation

The graphs show the noise parameters Amp and ϕ for the three components 50 Hz (a), 150 Hz (b) and 250 Hz (c). The parameters are extracted from fitting the CPMG scans (see figure 5.3). The scans were taken on different consecutive days (different colors and markers), as well as on the same day in the morning and afternoon (same color and marker). The error bars show the fit parameter errors.

5. Experimental compensation of magnetic field noise

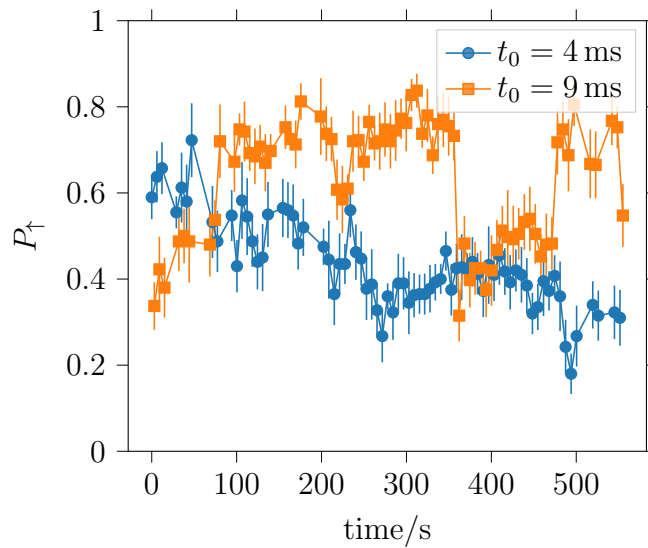


Figure 5.5.: Noise signal fluctuation

The graph shows the excitation of the CPMG sequence detecting the compensated 50 Hz noise at a delay from line trigger of $t_0 = 4 \text{ ms}$ in blue and $t_0 = 9 \text{ ms}$ in orange scanned over the time. The jumps of the excitation at the maximum point $t_0 = 9 \text{ ms}$ between ~ 0.3 and ~ 0.8 and at the starting point $t_0 = 4 \text{ ms}$ between ~ 0.2 and ~ 0.7 correspond to a fluctuation of the amplitude of the 50 Hz noise of $\Delta A = 50 \text{ s}^{-1}$ ($\Delta B = 2.8 \mu\text{G}$). The excitation is alternately measured every 2 s for a time span of 10 min. The data points show the mean over the ions and the error bars the standard deviations.

5. Experimental compensation of magnetic field noise

5.1.3. Characterisation and compensation of noise components using the 729-transition

The first trials of compensating and analysing the magnetic field noise were done with the optical qubit. The corresponding experiment sequence is illustrated in figure 5.6. Here the compensation was not performed with the iterative approach described in the chapter 5.1.1, but with trial and error. The strength of the noise is obtained by fitting the CPMG signal with equation (5.1). The RedPitaya is used to apply an out-of-phase signal based on the fitted amplitude and phase to the magnetic field coils. The fine tuning is performed by trial-and-error and remeasuring the remaining signal. The measurement data are shown in figure 5.7. The difference in amplitude and phase of the noise components measured with the ground state qubit (figure 5.3) can be explained by the fact that during this measurement the mu-metal shielding was not fully closed. Hence stronger magnetic field amplitudes for the 50 Hz and 250 Hz component of $B_{50\text{Hz}} = 37.2(5) \mu\text{G}$ and $B_{250\text{Hz}} = 23.3(6) \mu\text{G}$ are measured. For the 150 Hz a smaller noise amplitude of $B_{150\text{Hz}} = 9.3(8) \mu\text{G}$ is measured. The smaller overall contrast C compared to the measurements using the Raman transition is attributed to laser phase noise introduced by the 729 nm laser. The contrast also shows a dependence on the number of π -pulses. The contrast of the CPMG measurement with $N = 6$ pulses (5.7(b)) $C = 0.54$ is smaller than the contrast of the measurements with $N = 10$ ($C = 0.77$) and $N = 2$ ($C = 0.6$) pulses. It means that the CPMG measurements pick up additional line-asynchronous noise with frequency components, where they are sensitive to.

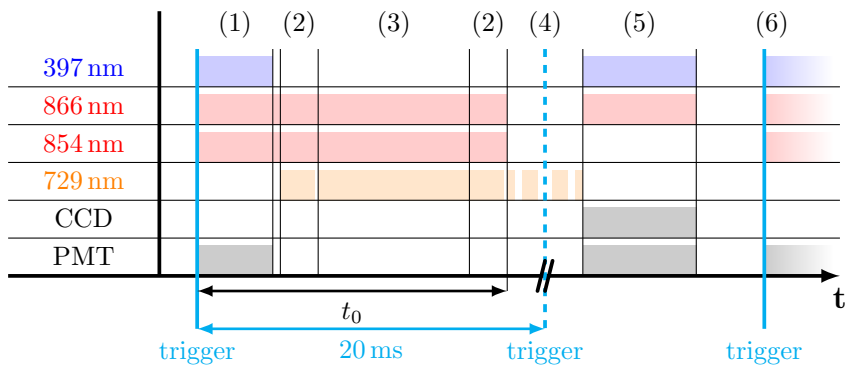


Figure 5.6.: Experiment sequence

The diagram shows the laser sequence for an experiment using the 729-transition. The steps are (1) Doppler cooling from 3 ms to 23 ms, (2) state preparation (0.1 ms), (3) sideband cooling (6 ms), (4) sequence (20 ms), (5) detection (5 ms) and (6) next measurement. t_0 is the time it takes from the trigger to the start of the pulse sequence.

5. Experimental compensation of magnetic field noise

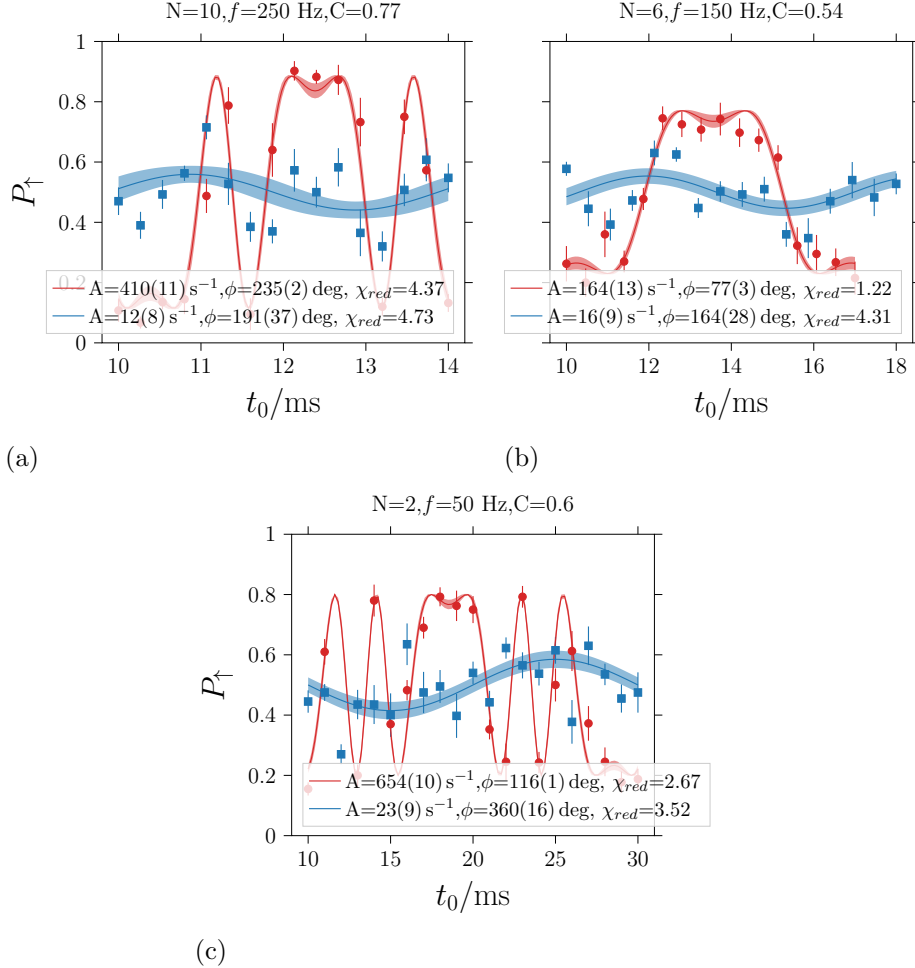


Figure 5.7.: Noise components before and after compensation using the 729-transition

The graphs show CPMG scans for the three noise components 250 Hz (a), 150 Hz (b) and 50 Hz (c). The red fit curves and data points show the magnetic field noise and the blue points and fit curves the remaining noise after compensating. The data points are the excitation averaged over the ions and the errorbars show the standard deviations. The blue and red band show one sigma confidence interval of the fit parameter errors.

5.1.4. Ramsey contrast with and without compensation

In order to observe if the compensation system adds noise, a Ramsey measurement by scanning the laser phase of the second $\frac{\pi}{2}$ -pulse is performed. The Ramsey contrast for a free evolution time of 4.5 ms is shown in figure 5.8. Using neither the compensation nor the line trigger (see blue curve in figure 5.8) results in a strongly reduced fringe contrast and also π phase shifted contrast fringe. For

5. Experimental compensation of magnetic field noise

the measurement using only the compensation system (green) the contrast is not reduced compared to the measurement with line trigger and compensation (red). This indicates that the compensation system does not add extra noise to the system. Based on this, it is not necessary anymore to use the line trigger for measurements. As a result the measurements directly start after each other and do not have to be paused until the next line trigger signal happens. This leads to a faster repetition rate of measurements. However, it has to be noted that the CCD camera relies on the trigger signal and does not work without line trigger. Taking a look at equation (3.16) the contrast can also become negative for strong magnetic field amplitudes, therefore the π phase shift in the measurement without compensation and line trigger. Using this equation a theoretical value of the reduced contrast (blue curve) can be calculated. Therefore the noise parameters of figure 5.7 are used and numerically integrating equation (3.16) gives a value of $C = -0.13$, which is approximately half the measured value of $C = -0.25(3)$. The difference between the simulated value and the measured one comes from the fact that only the line induced magnetic field noises are taken into account for the simulation. All other kinds of noises, which lead to the reduction of the Ramsey contrast are not included.

5. Experimental compensation of magnetic field noise

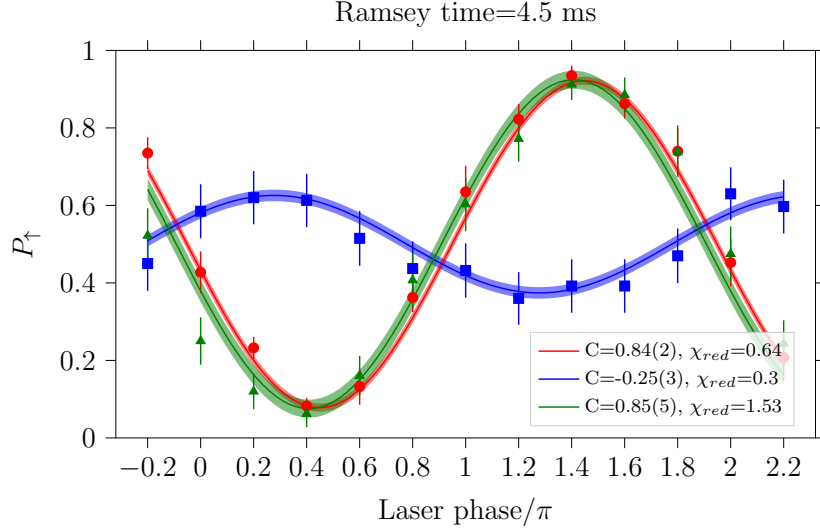


Figure 5.8.: Ramsey contrast with and without compensation

The data points show Ramsey measurements with a waiting time of 4.5 ms. The red data points are taken with the line trigger and the compensation on whereas the green data points are taken with the compensation on but the line trigger off. The blue data points show the measurement with the compensation as well as the line trigger off. The contrast is taken from the fit with formula (5.2). The data points, which are taken with the line trigger, are the average over 8 ions and the error bars are the standard deviations. For the measurements without line trigger the error bars are showing the quantum projection noise (2.9).

5.2. Compensation of magnetic field noise at the Precision experiment

After successfully implementing the compensation system at the QSIM experiment, the same system was also added to the Precision experiment. The first section discusses the measurements for the noise analysis and compensation. The second section presents the coherence time measurement with and without compensation system, whereby the Ramsey contrast is observed for different free evolution times.

5.2.1. Characterisation and compensation of noise components

The noise analysis and compensation was performed with the characterisation routine, described in chapter 5.1.1. Here only the differences to the measurements in the QSIM experiment are mentioned. The measurements are preformed with a single ion using the 729-transition as compared to 8 ions, which are used in the QSIM experiment. The scaling factor for the Precision experiment is

5. Experimental compensation of magnetic field noise

$k = 11200/5 \text{ V/G}$ in the amplitude equation (5.3). Measurements of the noise components before and after compensation are shown in figure 5.9. The observed magnetic strengths of the noise before compensation are $B_{50\text{Hz}} = 17.1(4) \mu\text{G}$, $B_{150\text{Hz}} = 9.8(7) \mu\text{G}$ and $B_{250\text{Hz}} = 6.2(6) \mu\text{G}$. The final remaining parts are $B_{50\text{Hz}} = 0.7(3) \mu\text{G}$, $B_{150\text{Hz}} = 2.1(34) \mu\text{G}$ and $B_{250\text{Hz}} = 1.5(3) \mu\text{G}$. The magnetic field strengths of the noise components are smaller than in the QSIM experimental setup. Also the higher harmonic components decrease in amplitude, whereas at the QSIM setup the 250 Hz component is second strongest. The best compensation is achieved for the 50 Hz component, see figure 5.9(f), whereas for the other components a compensation to $\sim 1/4$ of the amplitude is achieved.

5. Experimental compensation of magnetic field noise

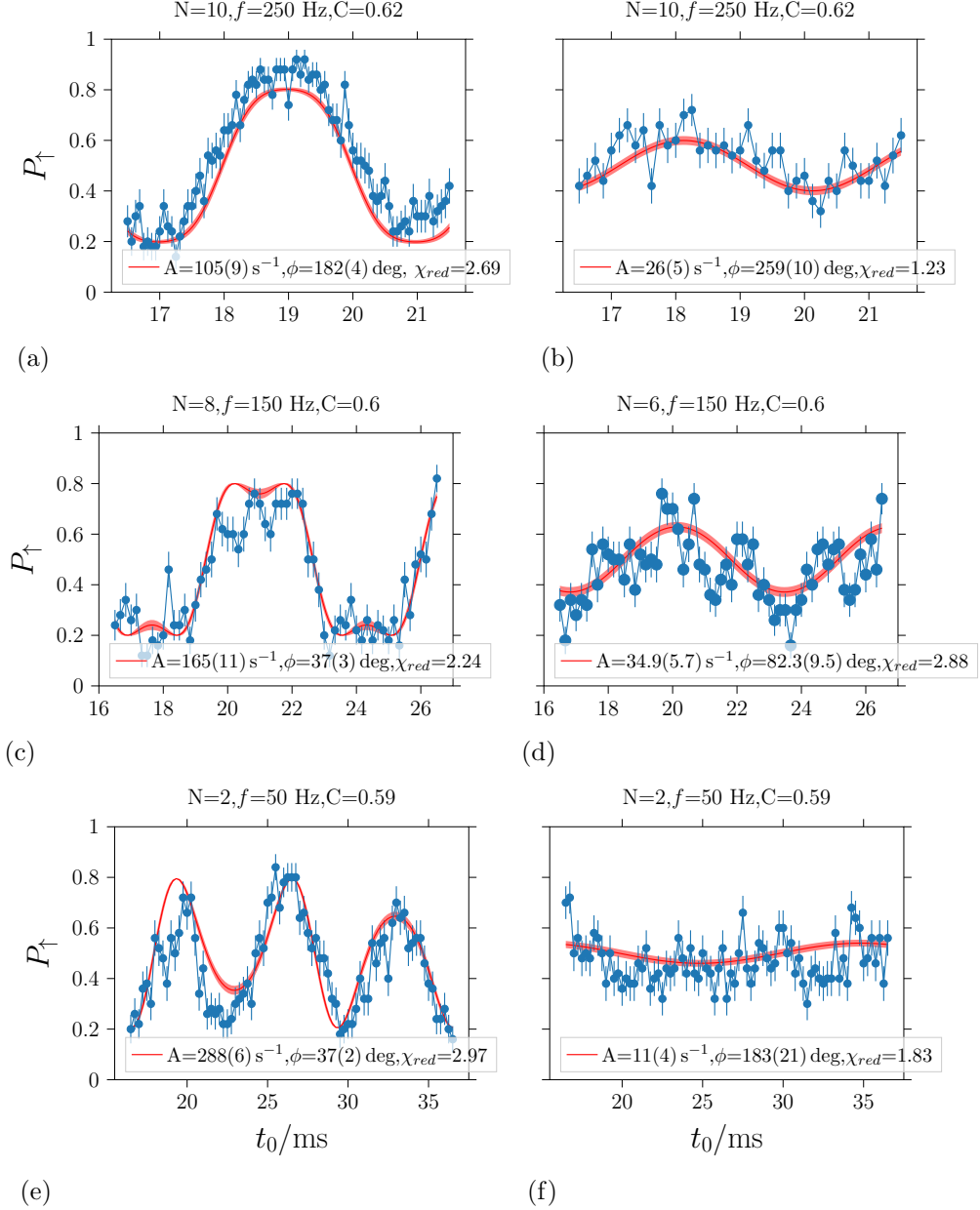


Figure 5.9.: Noise components before and after compensation at the Precision experiment

The graphs show the CPMG scans taken at the Precision experiment. (a) and (b) show the signal for 250 Hz before and after compensation. The 150 Hz signal before compensation is presented in (c) and after compensation in (d). The 50 Hz signal is shown in (e) and compensated in (f). For analysis of the noise parameters the data are fitted with formula (5.1) (red curves). The error bars are calculated from quantum projection noise (2.9).

5. Experimental compensation of magnetic field noise

5.2.2. Coherence measurement with Ramsey contrast

For analysing the coherence of the ion qubit at the Precision experiment with and without noise compensation, Ramsey experiments with different free evolution times are taken. The loss of contrast is then observed as a function of the Ramsey free evolution time, as shown in figure 5.10. The Ramsey measurements were performed between the states $D_{5/2}, m = -3/2 \leftrightarrow D_{5/2}, m = 5/2$. This transition has a twice as big magnetic sensitivity $\gamma \approx 4.8$ than the Raman or the 729-transition. The Ramsey measurements are done by applying a π -pulse from $S_{1/2}, m = 1/2 \rightarrow D_{5/2}, m = -3/2$ after the first $\pi/2$ -pulse and another one immediately before the last $\pi/2$ -pulse. The measurements are taken without line trigger. The loss of contrast without compensation is shown in figure 5.10 (a). The data points are obtained by fitting single Ramsey experiments with equation (3.16).¹ The black curve shows simulated data by numerical integration of equation (3.16) with the measured noise parameter from figure 5.9. The loss of contrast with the compensation system on is shown in figure 5.10(b). Here the simulation is done using the parameters of the remaining part of the noise components (see figure 5.9). In both cases the simulations do not fully fit the data points but matches the structure of the contrast loss. As described earlier, also other sources of noise, which are not covered by the simulation, are leading to a contrast loss.

¹In this fit the contrast parameter is fixed to be positive with an additional phase parameter in the fitting function.

5. Experimental compensation of magnetic field noise

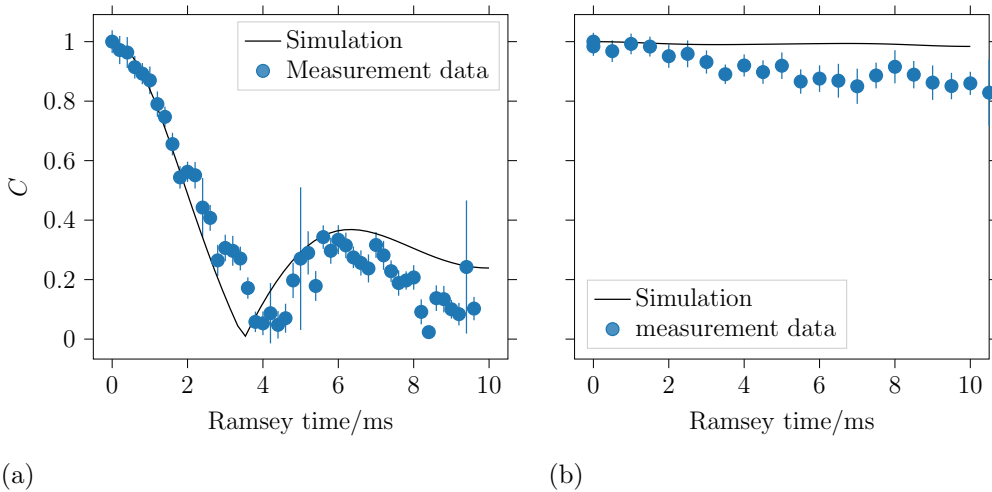


Figure 5.10.: Ramsey contrast for different Ramsey times

Figure (a) shows the contrast loss as a function of Ramsey time without compensation. The black curve shows a numerical simulation of formula (3.16) with the known noise parameters from figure 5.9. The loss of contrast with compensation is shown in figure (b). For the simulated black curve, the parameters of the remaining signal in figure 5.9 are used. The errorbars are the fit parameter errors.

6. Conclusion and outlook

The goal of this thesis was to develop a feed-forward magnetic field noise cancellation system for a trapped-ion quantum simulation experiment. The compensation system is used to suppress the ambient magnetic field noise in the laboratory. This magnetic field noise is induced by the 50 Hz power line. Magnetic field oscillations with higher harmonics of 50 Hz (especially odd multiples 150 Hz, 250 Hz ..) are also present in the lab. At first, a method to use the ion qubit as sensor to measure temporal magnetic field variations was introduced. Towards this end, a π -pulse sequence (CPMG sequence) is shifted over one cycle of the 50 Hz mains signal (period of 20 ms) by delaying the sequence from the trigger induced by the AC mains. Thereby the magnetic field oscillation is mapped to the ion's excitation and the amplitude and phase of the different frequency components of the magnetic field variation can be extracted. Depending on the number of π -pulses and the overall sequence length, the sequence can be engineered to be sensitive to a particular frequency component of the magnetic field noise. This experiment was performed on two different qubits: The ground state qubit of the Ca⁺ ion (Raman transition) and the optical qubit (729-transition). On the technical side, the feed-forward compensation system contains magnetic-field coils, which are already installed at the vacuum chamber of the trap, and a programmable RedPitaya board to drive the coils. For an easier operation of the RedPitaya, a control software with a user interface was developed. Additionally, the software includes a semi-automatic mode, where the magnetic field parameters are analysed by fitting the data of the π -pulse scan and the corresponding out-of phase signal to destructively superpose the magnetic noise and suppress the very same. With this compensation system it was possible to suppress the strength of the strongest noise component (the 50 Hz component) from $B = 28.1(2)$ μ G to $B = 1.6(3)$ μ G. In the measurement with a not fully closed mu-metal enclosure a magnetic field strength of the 50 Hz component of $B = 37.2(5)$ μ G was measured, which is approximately 9 μ G higher. To put these values in a context, the quantum optic experiment in [15] measured a magnetic field strength of the 50 Hz component of $B = 262(5)$ μ G. In another quantum optic experiment with trapped ions [39] they measured an attenuation, given by their two-layer mu-metal shield, of the magnetic field noise by 20 – 30 dB for the 50 – 100 Hz frequency components. Furthermore they measured remaining AC induced magnetic field noise at the ions in a similar measurement as we did. They compared the strengths of the remaining noise for

6. Conclusion and outlook

four different situations: The quantization axis generated by magnetic field coils and generated by Sm₂Co₁₇ permanent magnets as well as with a closed and open mu-metal shield respectively. In the case of using permanent magnets the remaining noise was $B = 8.9(2) \mu\text{G}$ (closed shield) and $B = 500(36) \mu\text{G}$ (open shield). The remaining noise for generating the quantization field with magnetic field coils was $B = 107(18) \mu\text{G}$ (closed shield) and $B = 893(72) \mu\text{G}$ (open shield). After the successful installation of the compensation system at the QSIM experiment, the same system was installed in the Precision experiment.

The next possible step would be to develop a fully-automated compensation routine. Until now the CPMG scan measurements to quantify the noise components have to be done manually. The idea would be that the RedPitaya communicates with the laboratory control computer, starts a CPMG measurement by itself and analyses the measurement data in the way described in this thesis. This process would have to be repeated to find the optimal compensation parameters and after successfully suppressing the magnetic field noise it would continue with the compensation of the next frequency component.

A. Derivation of the filter function

The π -pulse train with N π -pulses and sequence duration τ , assuming no time evolution during the π -pulse is represented by the operator

$$M = \mathcal{U}_R\left(\frac{\pi}{2}, \frac{\pi}{2}\right) \mathcal{U}_t(\delta_N, \delta_{N+1}\tau) \prod_{j \in \{1, \dots, N\}} [\mathcal{U}_R(\pi, \varphi_{l,j}) \mathcal{U}_t(\delta_{j-1}\tau, \delta_j\tau)] \mathcal{U}_R\left(\frac{\pi}{2}, 0\right)$$

with the operator $\mathcal{U}_t(\delta_{j-1}\tau, \delta_j\tau) = \exp\left(-i/2\sigma_z \int_{\delta_{j-1}\tau}^{\delta_j\tau} \Delta(t)dt\right)$ describing the free evolution between the j th pulse and the $(j-1)$ th pulse and the rotation operator $\mathcal{U}_R(\pi, \varphi_{l,j}) = -i(e^{-i\varphi_{l,j}}\sigma_+ + e^{i\varphi_{l,j}}\sigma_-) = -i\sigma_{\varphi_{l,j}}$ representing the j th π -pulse with a laser phase $\varphi_{l,j}$. The center of the j th π -pulse occurs at time $\tau_j = \delta_j\tau$, therefore $\delta_{N+1} = 1$ and $\delta_0 = 0$. The operator is then

$$\begin{aligned} M &= \mathcal{U}_R\left(\frac{\pi}{2}, \frac{\pi}{2}\right) e^{-i/2\sigma_z \int_{\delta_N\tau}^{\delta_{N+1}\tau} \Delta(t)dt} \\ &\cdot (-i)^N \prod_{j \in \{1, \dots, N\}} \left[\sigma_{\varphi_{l,j}} e^{-i/2\sigma_z \int_{\delta_{j-1}\tau}^{\delta_j\tau} \Delta(t)dt} \right] \mathcal{U}_R\left(\frac{\pi}{2}, 0\right), \end{aligned}$$

where $(-i)^N$ can be neglected as global phase. For simplification the factor of the product is rewritten

$$\begin{aligned} \sigma_{\varphi_{l,j}} e^{-i/2\sigma_z \int_{\delta_{j-1}\tau}^{\delta_j\tau} \Delta(t)dt} &= (e^{-i\varphi_{l,j}}\sigma_+ + e^{i\varphi_{l,j}}\sigma_-)(e^{-i/2\phi_j} |\uparrow\rangle\langle\uparrow| + e^{i/2\phi_j} |\downarrow\rangle\langle\downarrow|) \\ &= (e^{-i\varphi_{l,j}} |\uparrow\rangle\langle\downarrow| + e^{i\varphi_{l,j}} |\downarrow\rangle\langle\uparrow|)(e^{-i/2\phi_j} |\uparrow\rangle\langle\uparrow| + e^{i/2\phi_j} |\downarrow\rangle\langle\downarrow|) \\ &= e^{-i\varphi_{l,j} + i/2\phi_j} |\uparrow\rangle\langle\downarrow| + e^{i\varphi_{l,j} - i/2\phi_j} |\downarrow\rangle\langle\uparrow| \end{aligned}$$

with the phase $\phi_j = \int_{\delta_{j-1}\tau}^{\delta_j\tau} \Delta(t)dt$ and the operators $\sigma_+ = |\uparrow\rangle\langle\downarrow|$ and $\sigma_- = |\downarrow\rangle\langle\uparrow|$. Multiplying the j th and $(j+1)$ th factor results in

$$\begin{aligned} \sigma_{\varphi_{l,j+1}} e^{-i/2\phi_{j+1}\sigma_z} \sigma_{\varphi_{l,j}} e^{-i/2\phi_j\sigma_z} &= (e^{-i\varphi_{l,j+1} + i/2\phi_{j+1}} |\uparrow\rangle\langle\downarrow| + e^{i\varphi_{l,j+1} - i/2\phi_{j+1}} |\downarrow\rangle\langle\uparrow|) \\ &\cdot (e^{-i\varphi_{l,j} + i/2\phi_j} |\uparrow\rangle\langle\downarrow| + e^{i\varphi_{l,j} - i/2\phi_j} |\downarrow\rangle\langle\uparrow|) \\ &= e^{i/2(\phi_{j+1} - \phi_j) - i(\varphi_{l,j+1} - \varphi_{l,j})} |\uparrow\rangle\langle\uparrow| \\ &\quad + e^{-i/2(\phi_{j+1} - \phi_j) + i(-\varphi_{l,j+1} - \varphi_{l,j})} |\downarrow\rangle\langle\downarrow|. \end{aligned}$$

A. Derivation of the filter function

Using the already calculated factors the product is

$$\prod_{j \in \{1, \dots, N\}} \sigma_{\varphi_{l,j}} e^{-i/2\phi_j \sigma_z} = \begin{cases} e^{i/2 \sum_j^N (-1)^j \phi_j} e^{-i \sum_j^N (-1)^j \varphi_{l,j}} |\uparrow\rangle \langle \uparrow| \\ + e^{-i/2 \sum_j^N (-1)^j \phi_j} e^{i \sum_j^N (-1)^j \varphi_{l,j}} |\downarrow\rangle \langle \downarrow| \end{cases} \text{ for } N \text{ even} \\ \begin{cases} e^{i/2 \sum_j^N (-1)^j \phi_j} e^{-i \sum_j^N (-1)^j \varphi_{l,j}} |\downarrow\rangle \langle \uparrow| \\ - e^{-i/2 \sum_j^N (-1)^j \phi_j} e^{i \sum_j^N (-1)^j \varphi_{l,j}} |\uparrow\rangle \langle \downarrow| \end{cases} \text{ for } N \text{ odd.}$$

Rewriting the product with the accumulated phase $\phi = \sum_{j=1}^{N+1} (-1)^j \phi_j$ and the accumulated laser phase $\varphi_l = \sum_{j=1}^N (-1)^j \varphi_{l,j}$ gives

$$e^{-i/2\phi_{N+1}\sigma_z} \prod_{j \in \{1, \dots, N\}} \sigma_{\varphi_{l,j}} e^{-i/2\phi_j \sigma_z} = \begin{cases} e^{i/2\phi - i\varphi_l} |\uparrow\rangle \langle \uparrow| + e^{-i/2\phi + i\varphi_l} |\downarrow\rangle \langle \downarrow|, \text{ for } N \text{ even} \\ e^{i/2\phi - i\varphi_l} |\downarrow\rangle \langle \uparrow| - e^{-i/2\phi + i\varphi_l} |\uparrow\rangle \langle \downarrow|, \text{ for } N \text{ odd} \end{cases}.$$

Including the embedding operators, which represent the action of the two $\pi/2$ -pulses, gives the matrix M for even values of N

$$\begin{aligned} M &= \frac{1}{2} (\mathbb{I} - i\sigma_y) (e^{i/2\phi - i\varphi_l} |\uparrow\rangle \langle \uparrow| + e^{-i/2\phi + i\varphi_l} |\downarrow\rangle \langle \downarrow|) (\mathbb{I} - i\sigma_x) \\ &= \frac{1}{2} (|\uparrow\rangle \langle \uparrow| + |\downarrow\rangle \langle \downarrow| - |\uparrow\rangle \langle \downarrow| + |\downarrow\rangle \langle \uparrow|) (e^{i/2\phi - i\varphi_l} |\uparrow\rangle \langle \uparrow| + e^{-i/2\phi + i\varphi_l} |\downarrow\rangle \langle \downarrow|) \\ &\quad \cdot (|\uparrow\rangle \langle \uparrow| + |\downarrow\rangle \langle \downarrow| - i|\uparrow\rangle \langle \downarrow| - i|\downarrow\rangle \langle \uparrow|) \\ &= \frac{1}{2} ((e^{i/2\phi - i\varphi_l} + ie^{-i/2\phi + i\varphi_l}) |\uparrow\rangle \langle \uparrow| + (e^{i/2\phi - i\varphi_l} - ie^{-i/2\phi + i\varphi_l}) |\downarrow\rangle \langle \uparrow| \\ &\quad - (ie^{i/2\phi - i\varphi_l} + e^{-i/2\phi + i\varphi_l}) |\uparrow\rangle \langle \downarrow| + (-ie^{i/2\phi - i\varphi_l} + e^{-i/2\phi + i\varphi_l}) |\downarrow\rangle \langle \downarrow|). \end{aligned}$$

The probability P_\uparrow from the transition element $\langle \uparrow | M | \downarrow \rangle$, which can be extracted from the formula above, is

$$\begin{aligned} P_\uparrow &= |\langle \uparrow | M | \downarrow \rangle|^2 = \frac{1}{4} (ie^{i/2\phi - i\varphi_l} + e^{-i/2\phi + i\varphi_l}) (e^{i/2\phi - i\varphi_l} - ie^{-i/2\phi + i\varphi_l}) \\ &= \frac{1}{4} (1 + 1 - ie^{-i\phi + 2i\varphi_l} + ie^{i\phi - 2i\varphi_l}) \\ &= \frac{1}{2} - \frac{1}{2} \sin(\phi - 2\varphi_l). \end{aligned}$$

The case of N odd gives the same transition element and the same formula for P_\uparrow . The probability also depends on the accumulated laser phase φ_l . Fixing the phase of the individual π -pulses $\varphi_{l,j}$ to the same value leads to a zero accumulated laser phase $\varphi_l = 0$. In the experiment described in this work, alternating laser phases $\varphi_{l,j} = \pm \frac{\pi}{2}$ were used. In the case of general alternating laser phases, which are

A. Derivation of the filter function

chosen the way that $|\varphi_{l,j+1} - \varphi_{l,j}| = \pi$, the accumulate laser phase is $|\varphi_l| = N\pi$. Both cases deliver the simplified formula

$$P_\uparrow = \frac{1}{2} - \frac{1}{2} \sin(\phi).$$

For more complicated variations of laser phases the accumulated laser phase has to be calculated.

The accumulated phase

$$\phi = \int_0^\tau \mathcal{F}(t) \Delta(t) dt$$

can be written with a filter function, which is defined in the time domain

$$\mathcal{F}(t) = \begin{cases} 0, & t < 0 \\ (-1)^j, & \delta_j \tau \leq t < \delta_{j+1} \tau \text{ between } \pi\text{-pulses} \\ 0, & t \geq \tau \end{cases} \quad (\text{A.1})$$

and in the frequency domain

$$\begin{aligned} \phi &= \int_0^\tau \mathcal{F}(t) \Delta(t) dt = \int_{-\infty}^\infty \mathcal{F}(t) \Delta(t) dt \\ &= \int_{-\infty}^\infty \Delta(t) \frac{1}{\sqrt{2\pi}} \int_{-\infty}^\infty \tilde{\mathcal{F}}(\omega) e^{i\omega t} d\omega dt \\ &= \int_{-\infty}^\infty \tilde{\mathcal{F}}(\omega) \frac{1}{\sqrt{2\pi}} \int_{-\infty}^\infty \Delta(t) e^{i\omega t} dt d\omega \\ &= \int_{-\infty}^\infty \tilde{\mathcal{F}}(\omega) \frac{1}{\sqrt{2\pi}} \left[\int_{-\infty}^\infty \Delta(t) e^{-i\omega t} dt \right]^* d\omega \\ &= \int_{-\infty}^\infty \tilde{\mathcal{F}}(\omega) \tilde{\Delta}^*(\omega) d\omega. \end{aligned}$$

If the experiment does not start at a time $t_0 = 0$ the time translation $\mathcal{F}(t + t_0)$ has to be modified to

$$\int_{-\infty}^\infty \tilde{\mathcal{F}}(\omega) \tilde{\Delta}^*(\omega) e^{i\omega t_0} d\omega.$$

Assuming noise made up of discrete components in the frequency domain

$$\begin{aligned} \Delta(t) &= \sum_j \Delta_j \sin(\omega_j t + b_j) \\ \tilde{\Delta}(\omega) &= \sum_j \frac{\sqrt{2\pi}}{2i} \Delta_j (e^{ib_j} \delta(\omega - \omega_j) - e^{-ib_j} \delta(\omega + \omega_j)) \end{aligned}$$

A. Derivation of the filter function

and using the filter function in frequency domain,

$$\begin{aligned}
\tilde{\mathcal{F}}(\omega) &= \frac{1}{\sqrt{2\pi}} \left[-\frac{1}{i\omega} (e^{i\omega\delta_1\tau} - 1) + \frac{1}{i\omega} (e^{i\omega\delta_2\tau} - e^{i\omega\delta_1\tau}) + \dots - \frac{(-1)^N}{i\omega} (e^{i\omega\delta_{N+1}\tau} - e^{i\omega\delta_N\tau}) \right] \\
&= \frac{1}{\sqrt{2\pi}i\omega} [1 - 2e^{i\omega\delta_1\tau} + 2e^{i\omega\delta_2\tau} \dots + (-1)^N e^{i\omega\delta_N\tau} + (-1)^{N+1} e^{i\omega\delta_{N+1}\tau}] \\
&= \frac{1}{\sqrt{2\pi}i\omega} \left[1 + (-1)^{N+1} e^{i\omega\tau} + 2 \sum_{j=1}^N (-1)^j e^{i\omega\tau\delta_j} \right],
\end{aligned}$$

the accumulated phase can be finally expressed as

$$\begin{aligned}
\phi &= \int_{-\infty}^{\infty} \tilde{\mathcal{F}}(\omega) \tilde{\Delta}^*(\omega) e^{-i\omega t_0} d\omega \\
&= \sum_j \frac{\sqrt{2\pi}}{2i} \Delta_j \left(e^{ib_j} \int_{-\infty}^{\infty} \tilde{\mathcal{F}}(\omega) \delta(\omega - \omega_j) e^{i\omega t_0} d\omega - e^{-ib_j} \int_{-\infty}^{\infty} \tilde{\mathcal{F}}(\omega) \delta(\omega + \omega_j) e^{i\omega t_0} d\omega \right) \\
&= \sum_j \frac{\sqrt{2\pi}}{2i} \Delta_j \left(e^{ib_j} \tilde{\mathcal{F}}(\omega_j) e^{i\omega_j t_0} - e^{-ib_j} \tilde{\mathcal{F}}(-\omega_j) e^{-i\omega_j t_0} \right) \\
&= \sum_j \frac{\sqrt{2\pi}}{2i} \Delta_j \left(\tilde{\mathcal{F}}(\omega_j) e^{i(\omega_j t_0 + b_j)} - c.c. \right) \\
&= \sum_j \frac{\sqrt{2\pi}}{2i} \Delta_j |\tilde{\mathcal{F}}(\omega_j)| \left(e^{i(\omega_j t_0 + b_j + \arg(\tilde{\mathcal{F}}(\omega_j)))} - c.c. \right) \\
&= \sum_j \sqrt{2\pi} \Delta_j |\tilde{\mathcal{F}}(\omega_j)| \sin \left(\omega_j t_0 + b_j + \arg(\tilde{\mathcal{F}}(\omega_j)) \right)
\end{aligned}$$

in this derivation, the Fourier transformation

$$\tilde{f}(\omega) = \frac{1}{\sqrt{2\pi}} \int_{-\infty}^{\infty} e^{-i\omega t} f(t) dt$$

is used and the condition for the filter function,

$$\tilde{\mathcal{F}}(-\omega) = \tilde{\mathcal{F}}^*(\omega).$$

B. Controlling software for the Red Pitaya

The controlling software of the RedPitaya board is programmed in python. The graphic user interface (GUI) is created using the **Tkinter** binding. In the back end, the library **redpitaya_scpi** is used to communicate with the RedPitaya board and to send the strings including the SCPI commands to the RedPitaya board. The GUI includes three main windows: The interface for operating in manual mode (see figure B.1), the interface for automated fit (see figure B.2) and the window showing the parameters (see figure B.2). In order to be able to run the control software on any laboratory Windows PC, independent of the pre-installed python versions and libraries, a standalone program (executable file) is build out of the python program. Therefore the open-source module **cx_Freeze** is used to create the standalone program.

B.1. Controlling software: Manual mode

In the manual operation the parameters *frequency* (in Hz), *amplitude* (in mV), *phase* (in deg) of multiple sinusoidal functions and a general *offset* (in mV) can be set manually. By pressing the **Start** button the program sends a data string to the RedPitaya and the corresponding signal is applied at both outputs. The **Stop** button stops the operation. With the **Save parameters** button the entered values are saved in a txt file from which the values can also be loaded with the **Reset parameters** button. One can choose between an internal trigger (INT) and external trigger (EXT_PE for the positive edge of the external trigger signal and EXT_NE for the negative edge) on which the RedPitaya generates the signal.

The very right panel shows the RedPitaya IP address, which can be manually adjusted, in case the RedPitaya board is exchanged by another board with a different IP address. The panel also includes a message box. The messages include error information, for example if the connection to the RedPitaya failed or if the applied amplitude is bigger/smaller than ± 1 V.

B. Controlling software for the Red Pitaya

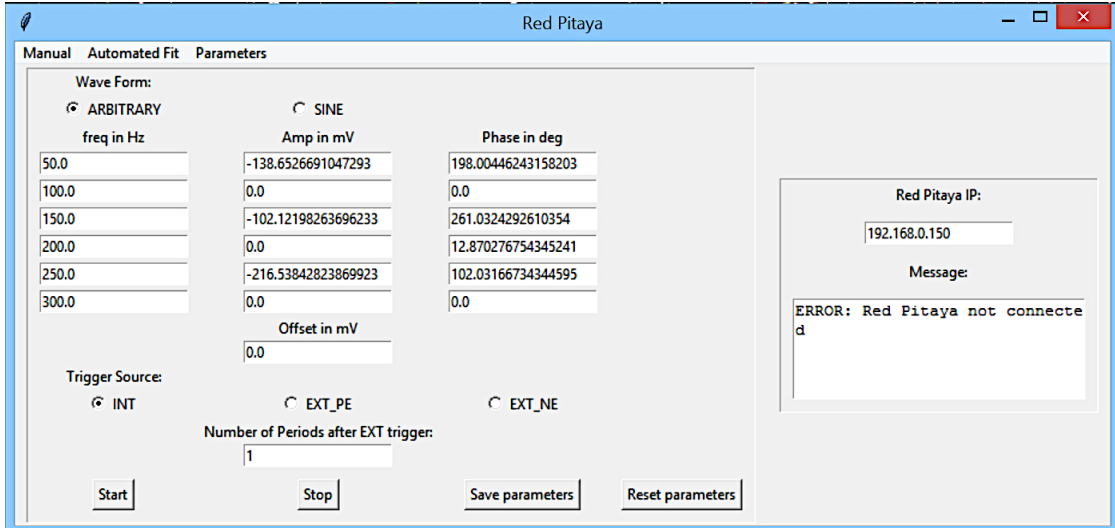


Figure B.1.: Controlling software: Manual window

The picture shows the interface of the RedPitaya controlling software in manual operation mode. For details see text.

B.2. Controlling software: Automated fit

In the automated fit mode (see picture B.2) it is possible to fit CPMG scan data. The data are loaded by setting the date and the filename (which is the time when the data was taken in the QSIM and Precision experiment). Then the fixed parameters, the noise frequency f and number of π -pulses as well as the fit contrast C are selected. The fit contrast can be selected between the two values for measurements taken with the Raman transition (refer to chapter 5.1.1) or the 729-transition (refer to chapter 5.1.3). Additionally a time off-set and the CPMG sequence length τ can be selected. By pressing the **Fit** button the data set is fitted with equation (5.1) using the selected fixed parameters. The fit result is shown in a pop-up window including a graph as shown in figure B.2(b). The graph includes the data points with error bars in blue, in case of measurements with multiple ions one data point is the average over the ions and the error bar the standard deviation, in measurements with a single ion the error bar shows the quantum projection noise. Also shown in the graph are the orange dashed curve the initial guess and the final fit in red. The legend presents the fit parameters amplitude Amp and phase ϕ and the fixed parameters number of π -pulses N , frequency f and the contrast as well as the goodness of the fit the reduced chi-squared χ_{red} . The button **Apply** applies the corresponding signal with the parameters gained from the fit at the RedPitaya. With the button **Measure** the compensation of the selected frequency component is shut down whereas the compensations of the other

B. Controlling software for the Red Pitaya

frequency components are still running. This allows a CPMG measurement of one frequency component, where the other frequency components are suppressed. The buttons **Start**, **Save** and **Reset parameters** as well as the very right panel are the same as in the manual mode.

Because of the complicated structure of the fit function (5.1) the success of the fit strongly depends on the initial guess. As the modification and the adding of electrical devices in the laboratory leads to random change of the magnetic field noise, the initial guess of the parameters can not be based on the already known parameters. To overcome this problem the initial guesses for the fit parameters are randomly chosen and the data are fitted. Based on the goodness of the fit, the fit is accepted or new random parameters are chosen and the fit repeated. This whole routine is automated. As value for the goodness of the fit the reduced chi-squared

$$\chi_{red} = \sum_i \frac{(fit_i - data_i)^2}{err_i^2} \quad (\text{B.1})$$

is calculated. Here the fit value is denoted with fit_i and the corresponding data point $data_i$ with its error err_i . Experience shows that values of $\chi_{red} < 6$ are good for accepting the fit. If the data set is not successfully fitted, the fit routine stops after 400 iterations.

B. Controlling software for the Red Pitaya

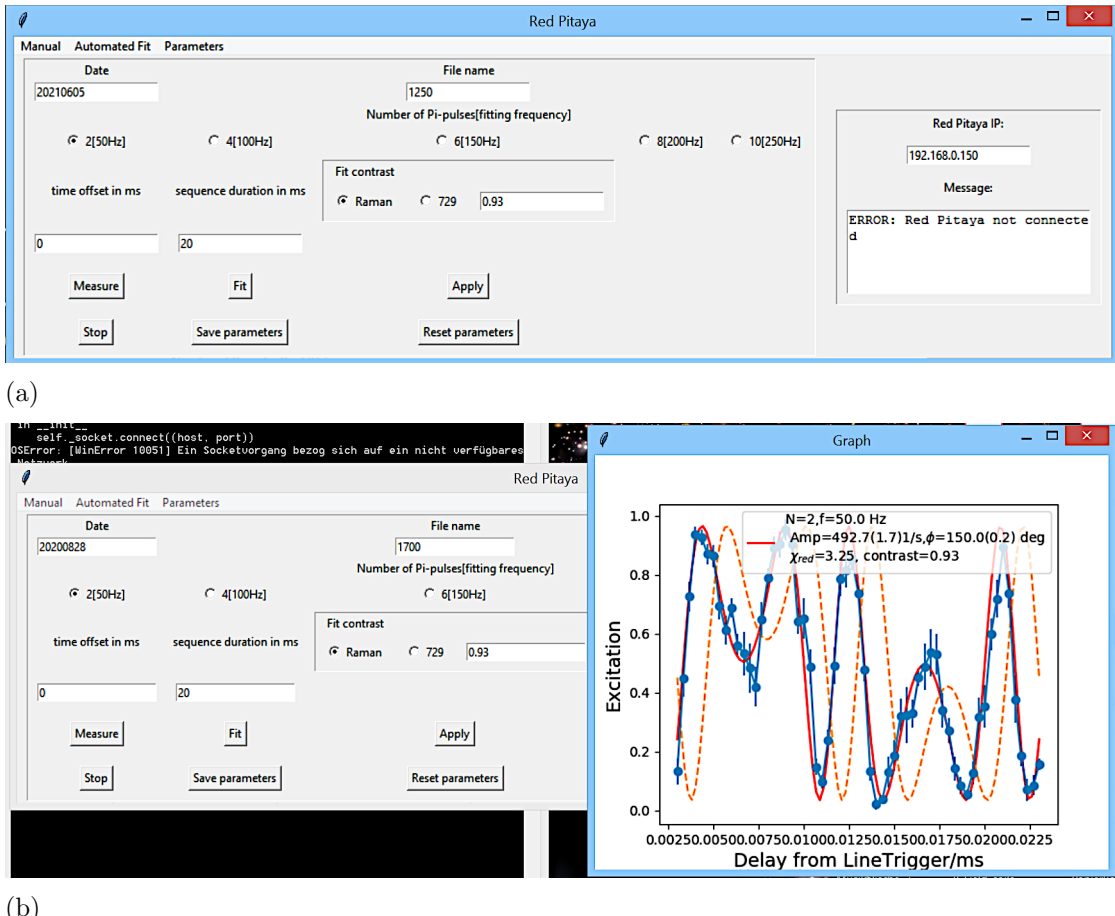


Figure B.2.: Controlling software: Automated Fit window

The pictures show the user interface of the Automated fit mode. Picture (b) shows the pop-up window including an example graph. For details see text.

B. Controlling software for the Red Pitaya

B.3. Controlling software: Parameter window

The Parameter window presents the fixed parameters, which are used for the automated fit mode. It lists the fit contrast C for the Raman and 729-transition for the different frequencies. It also includes the amp factor a and the phase shift ϕ_{shift} (refer to compensation routine presented in chapter 5.1.1). The parameters can be manipulated and saved to a txt file, as well as loaded from the very same.

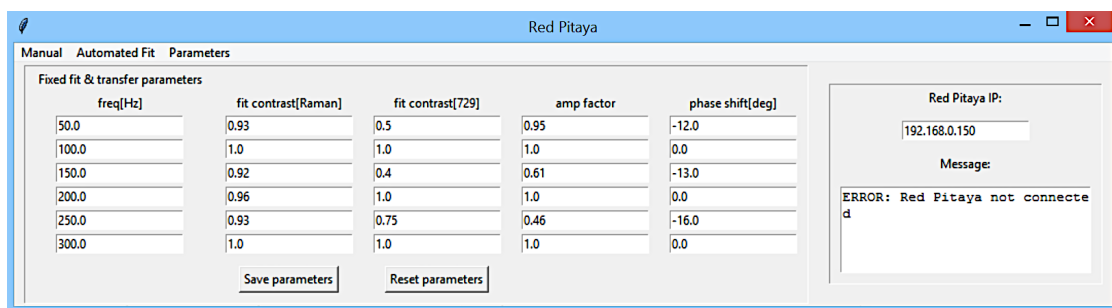


Figure B.3.: Controlling software: Parameter window

The picture shows the interface of the Parameter window. For details see text.

C. Useful Formulas

C.1. Trigonometric functions

Harmonic addition theorem [40]:

$$\sum_i a_i \sin(\omega t + \phi_i) = a \sin(\omega t + \phi)$$

with

$$a^2 = \sum_{i,j} a_i a_j \cos(\phi_i - \phi_j)$$

$$\phi = \text{atan} 2 \left(\frac{\sum_i a_i \sin(\phi_i)}{\sum_i a_i \cos(\phi_i)} \right)$$

C.2. Pauli matrices

Eigenvectors:

$$|\downarrow\rangle = \begin{pmatrix} 0 \\ 1 \end{pmatrix}, |\uparrow\rangle = \begin{pmatrix} 1 \\ 0 \end{pmatrix}$$

$$|+\rangle_x = \frac{1}{\sqrt{2}} \begin{pmatrix} 1 \\ 1 \end{pmatrix} = \frac{|\uparrow\rangle + |\downarrow\rangle}{\sqrt{2}}, |-\rangle_x = \frac{1}{\sqrt{2}} \begin{pmatrix} 1 \\ -1 \end{pmatrix} = \frac{|\uparrow\rangle - |\downarrow\rangle}{\sqrt{2}}$$

$$|+\rangle_y = \frac{1}{\sqrt{2}} \begin{pmatrix} 1 \\ i \end{pmatrix}, |-\rangle_y = \frac{1}{\sqrt{2}} \begin{pmatrix} 1 \\ -i \end{pmatrix} = \frac{|\uparrow\rangle - i|\downarrow\rangle}{\sqrt{2}}$$

Rotation operator:

$$\mathcal{U}_\varphi \left(\frac{\pi}{2}, 0 \right) = \frac{1}{\sqrt{2}} (\mathbb{I} - i\sigma_x)$$

$$\mathcal{U}_\varphi \left(\frac{\pi}{2}, \frac{\pi}{2} \right) = \frac{1}{\sqrt{2}} (\mathbb{I} - i\sigma_y)$$

$$\mathcal{U}_\varphi \left(\frac{\pi}{2}, \pi \right) = \frac{1}{\sqrt{2}} (\mathbb{I} + i\sigma_x)$$

$$\mathcal{U}_\varphi \left(\frac{\pi}{2}, \frac{3\pi}{2} \right) = \frac{1}{\sqrt{2}} (\mathbb{I} + i\sigma_y)$$

C. Useful Formulas

$$e^{i\frac{\theta}{2}\sigma_i}\sigma_j e^{-i\frac{\theta}{2}\sigma_i} = \cos(\theta)\sigma_j + \frac{i}{2}\sin(\theta)[\sigma_i, \sigma_j]$$

$$e^{i\frac{\theta}{2}\sigma_i}\sigma_{\pm} e^{-i\frac{\theta}{2}\sigma_i} = e^{\pm i\theta}\sigma_{\pm}$$

Euler's Formula

$$e^{ia(\hat{n}\cdot\vec{\sigma})} = \mathbb{I} \cos(a) + i(\hat{n}\cdot\vec{\sigma}) \sin(a) \quad (\text{C.1})$$

$$[\sigma_i, \sigma_j] = 2i\epsilon_{ijk}\sigma_k \quad (\text{C.2})$$

Baker-Campbell-Hausdorff-formula

$$e^A e^B = e^{A+B} e^{[A,B]/2} \quad (\text{C.3})$$

valid if $[A, B]$ commute with A, B .

C.3. Annihilation and creation operator

$$e^{i\theta a^\dagger a} a e^{-i\theta a^\dagger a} = e^{-i\theta} a \quad (\text{C.4})$$

$$e^{i\theta a^\dagger a} a^\dagger e^{-i\theta a^\dagger a} = e^{i\theta} a^\dagger \quad (\text{C.5})$$

$$e^{i\theta a^\dagger a} e^{i\eta(a+a^\dagger)} e^{-i\theta a^\dagger a} = e^{i\eta(ae^{-i\theta} + a^\dagger e^{i\theta})} \quad (\text{C.6})$$

$$e^{i\eta(a+a^\dagger)} = e^{-\eta^2/2} e^{i\eta a^\dagger} e^{i\eta a} \quad (\text{C.7})$$

List of Figures

2.1.	Linear Paul trap	11
2.2.	Bloch sphere	13
2.3.	Rotation on the Bloch sphere	14
2.4.	Level diagram of two-level system and QM harmonic oscillator	17
2.5.	Partial level diagram of Ca^+	19
2.6.	Mechanism of laser cooling	21
2.7.	Laser cooling of Ca^+	22
3.1.	Pulse sequence of a Ramsey experiment and state evolution on a Bloch sphere	26
3.2.	Simulation of line cycle measurement	27
3.3.	π -pulse train	28
3.4.	CPMG sequence	30
3.5.	Filter function of CPMG sequence	32
3.6.	Simulation of a CPMG scan	32
3.7.	Contrast fringes	34
4.1.	QSIM chamber with laser directions	36
4.2.	Photos of QSIM and Precision setup	37
4.3.	Magnetic field coils geometry	38
4.4.	B-field of coils	39
4.5.	Hardware of feed-forward system for noise cancellation	40
4.6.	Software of feed-forward system for noise cancellation	41
5.1.	Raman experiment sequence	43
5.2.	Compensation routine	46
5.3.	Noise components before and after compensation by magnetic field sensing using CPMG sequences on the Raman transition	47
5.4.	Noise parameter fluctuation	49
5.5.	Noise signal fluctuation	50
5.6.	Experiment sequence	51
5.7.	Noise components before and after compensation using the 729-transition	52
5.8.	Ramsey contrast with and without compensation	54

List of Figures

5.9. Noise components before and after compensation at the Precision experiment	56
5.10. Ramsey contrast for different Ramsey times	58
B.1. Controlling software: Manual window	66
B.2. Controlling software: Automated Fit window	68
B.3. Controlling software: Parameter window	69

Bibliography

- [1] Richard Phillips Feynman. Simulating Physics with Computers. *International Journal of Theoretical Physics*, 21:467488, 1982.
- [2] Tomi H. Johnson, Stephen R. Clark, and Dieter Jaksch. What is a quantum simulator? *EPJ Quantum Technology*, 1(1):10, Jul 2014.
- [3] R. Blatt and C. F. Roos. Quantum simulations with trapped ions. *Nature Physics*, 8(4):277–284, Apr 2012.
- [4] Immanuel Bloch, Jean Dalibard, and Sylvain Nascimbene. Quantum simulations with ultracold quantum gases. *Nature Physics*, 8(4):267–276, 2012.
- [5] M. Dalmonte, S. I. Mirzaei, P. R. Muppalla, D. Marcos, P. Zoller, and G. Kirchmair. Realizing dipolar spin models with arrays of superconducting qubits. *Phys. Rev. B*, 92:174507, Nov 2015.
- [6] Iulia Buluta and Franco Nori. Quantum Simulators. *Science*, 326(5949):108–111, 2009.
- [7] B. P. Lanyon, C. Hempel, D. Nigg, M. Müller, R. Gerritsma, F. Zähringer, P. Schindler, J. T. Barreiro, M. Rambach, G. Kirchmair, M. Hennrich, P. Zoller, R. Blatt, and C. F. Roos. Universal Digital Quantum Simulation with Trapped Ions. *Science*, 334(6052):57–61, 2011.
- [8] J. I. Cirac and P. Zoller. Quantum Computations with Cold Trapped Ions. *Phys. Rev. Lett.*, 74:4091–4094, May 1995.
- [9] C. Monroe, D. M. Meekhof, B. E. King, W. M. Itano, and D. J. Wineland. Demonstration of a Fundamental Quantum Logic Gate. *Phys. Rev. Lett.*, 75:4714–4717, Dec 1995.
- [10] D. J. Wineland, J. C. Bergquist, Wayne M. Itano, J. J. Bollinger, and C. H. Manney. Atomic-Ion Coulomb Clusters in an Ion Trap. *Phys. Rev. Lett.*, 59:2935–2938, Dec 1987.

Bibliography

- [11] Ferdinand Schmidt-Kaler, Hartmut Häffner, Mark Riebe, Stephan Gulde, Gavin PT Lancaster, Thomas Deuschle, Christoph Becher, Christian F Roos, Jürgen Eschner, and Rainer Blatt. Realization of the Cirac–Zoller controlled-NOT quantum gate. *Nature*, 422(6930):408–411, 2003.
- [12] Christian F. Roos, Mark Riebe, Hartmut Häffner, Wolfgang Hänsel, Jan Benhelm, Gavin P. T. Lancaster, Christoph Becher, Ferdinand Schmidt-Kaler, and Rainer Blatt. Control and Measurement of Three-Qubit Entangled States. *Science*, 304(5676):1478–1480, 2004.
- [13] M. K. Joshi, F. Kranzl, A. Schuckert, I. Lovas, C. Maier, R. Blatt, M. Knap, and C. F. Roos. Observing emergent hydrodynamics in a long-range quantum magnet, 2021. arXiv: 2107.00033.
- [14] Jos Arrillaga and Neville R. Watson. *Power system harmonics*. John Wiley & Sons, 2004.
- [15] B. Merkel, K. Thirumalai, J.E. Tarlton, V. M. Schäfer, C. J. Ballance, T. P. Harty, and D. M. Lucas. Magnetic field stabilization system for atomic physics experiments. *Review of Scientific Instruments*, 90(4):044702, 2019.
- [16] S. Meiboom and D. Gill. Modified Spin-Echo Method for Measuring Nuclear Relaxation Times. *Review of Scientific Instruments*, 29(8):688–691, 1958.
- [17] Wolfgang Paul. Electromagnetic traps for charged and neutral particles. *Rev. Mod. Phys.*, 62:531–540, Jul 1990.
- [18] C. Hempel. *Digital quantum simulation, Schrödinger cat state spectroscopy and setting up a linear ion trap*. PhD thesis, Universität Innsbruck, Available at <https://quantumoptics.at>, 2014.
- [19] P. Jurcevic. *Quantum Computation and Many-Body Physics with Trapped Ions*. PhD thesis, Universität Innsbruck, Available at <https://quantumoptics.at>, 2017.
- [20] Dietrich Leibfried, Rainer Blatt, Christopher Monroe, and David Wineland. Quantum dynamics of single trapped ions. *Reviews of Modern Physics*, 75(1):281, 2003.
- [21] Pradip K. Ghosh. *Ion traps*. Oxford University Press, 1995.
- [22] Pauli Virtanen, Ralf Gommers, Travis E. Oliphant, Matt Haberland, Tyler Reddy, David Cournapeau, Evgeni Burovski, Pearu Peterson, Warren Weckesser, Jonathan Bright, Stéfan J. van der Walt, Matthew Brett, Joshua

Bibliography

- Wilson, K. Jarrod Millman, Nikolay Mayorov, Andrew R. J. Nelson, Eric Jones, Robert Kern, Eric Larson, C. J. Carey, İlhan Polat, Yu Feng, Eric W. Moore, Jake VanderPlas, Denis Laxalde, Josef Perktold, Robert Cimrman, Ian Henriksen, E. A. Quintero, Charles R. Harris, Anne M. Archibald, Antônio H. Ribeiro, Fabian Pedregosa, Paul van Mulbregt, and SciPy 1.0 Contributors. SciPy 1.0: Fundamental Algorithms for Scientific Computing in Python. *Nature Methods*, 17:261–272, 2020.
- [23] Michael A. Nielsen and Isaac L. Chuang. *Quantum Computation and Quantum Information*. Cambridge University Press, 7th edition, 2010.
 - [24] W. M. Itano, J. C. Bergquist, J. J. Bollinger, J. M. Gilligan, D. J. Heinzen, F. L. Moore, M. G. Raizen, and D. J. Wineland. Quantum projection noise: Population fluctuations in two-level systems. *Phys. Rev. A*, 47:3554–3570, May 1993.
 - [25] J. J. Sakurai and Jim Napolitano. *Modern Quantum Mechanics*. Cambridge University Press, 2nd edition, 2017.
 - [26] C. F. Roos. *Controlling the quantum state of trapped ions*. PhD thesis, Universität Innsbruck, Available at <https://quantumoptics.at>, 2000.
 - [27] NIST. Atomic Data for Calcium (Ca). <https://physics.nist.gov/PhysRefData/Handbook/Tables/calciumentable1.htm>. Accessed: 2021-11-18.
 - [28] Stig Stenholm. The semiclassical theory of laser cooling. *Reviews of modern physics*, 58(3):699, 1986.
 - [29] Jürgen Eschner, Giovanna Morigi, Ferdinand Schmidt-Kaler, and Rainer Blatt. Laser cooling of trapped ions. *JOSA B*, 20(5):1003–1015, 2003.
 - [30] Götz S. Uhrig. Keeping a quantum bit alive by optimized π -pulse sequences. *Physical Review Letters*, 98(10):100504, 2007.
 - [31] E. L. Hahn. Spin Echoes. *Phys. Rev.*, 80:580–594, Nov 1950.
 - [32] Lorenza Viola and Seth Lloyd. Dynamical suppression of decoherence in two-state quantum systems. *Phys. Rev. A*, 58:2733–2744, Oct 1998.
 - [33] Michael J. Biercuk, Hermann Uys, Aaron P. VanDevender, Nobuyasu Shiga, Wayne M. Itano, and John J. Bollinger. Optimized dynamical decoupling in a model quantum memory. *Nature*, 458(7241):996–1000, 2009.

Bibliography

- [34] Jonas Bylander, Simon Gustavsson, Fei Yan, Fumiki Yoshihara, Khalil Harabi, George Fitch, David G. Cory, Yasunobu Nakamura, Jaw-Shen Tsai, and William D. Oliver. Noise spectroscopy through dynamical decoupling with a superconducting flux qubit. *Nature Physics*, 7(7):565–570, 2011.
- [35] Shlomi Kotler, Nitzan Akerman, Yinnon Glickman, and Roee Ozeri. Nonlinear single-spin spectrum analyzer. *Physical Review Letters*, 110(11):110503, 2013.
- [36] Michael J. Biercuk, Hermann Uys, Aaron P. VanDevender, Nobuyasu Shiga, Wayne M. Itano, and John J. Bollinger. Experimental Uhrig dynamical decoupling using trapped ions. *Physical Review A*, 79(6):062324, 2009.
- [37] M. Guggemos. *Precision spectroscopy with trapped $^{40}\text{Ca}^+$ and $^{27}\text{Al}^+$ ions*. PhD thesis, Universität Innsbruck, Available at <http://quantumoptics.at>, 2017.
- [38] Red pitaya documentation. <https://redpitaya.readthedocs.io/en/latest/appsFeatures/remoteControl/remoteControl.html>. Accessed: 2021-11-18.
- [39] Thomas Ruster, Christian T. Schmiegelow, Henning Kaufmann, Claudia Warschburger, Ferdinand Schmidt-Kaler, and Ulrich G. Poschinger. A long-lived zeeman trapped-ion qubit. *Applied Physics B*, 122(10):1–7, 2016.
- [40] Eric W. Weisstein. Harmonic addition theorem. From MathWorld—A Wolfram Web Resource. <https://mathworld.wolfram.com/HarmonicAdditionTheorem.html>. Accessed: 2021-11-18.